Investigation of the Electronic Structure and Magnetic Properties of CeO_{2-X}

by

Scott Zorn

A thesis

presented to the University of Waterloo

in fulfillment of the

thesis requirement for the degree of

Master of Science

in

Chemistry

Waterloo, Ontario, Canada, 2023

Author's Declaration

I hereby declare that I am the sole author of this thesis. This is a true copy of the thesis, including any required final revisions, as accepted by my examiners.

I understand that my thesis may be made electronically available to the public.

Abstract

In literature, it has been reported that undoped CeO_2 exhibits a room-temperature ferromagnetic-like ordering that does not follow Curie-type behaviour, typically found in magnetic materials. However, none of the proposed mechanisms have yet to be proven experimentally. So, the goal of this thesis was to study the magnetic and magneto-optical properties of CeO_2 to determine the potential mechanism causing the ferromagnetic-like ordering. This was done by systematically annealing undoped CeO_2 from nanocrystals (NCs) into bulk powders under different annealing time, temperature, and atmosphere to observe grain size and defect concentration impacts on the magnetic properties. Structural characterization, optical, magnetic, and magneto-optical measurements were then conduct on colloidal CeO_{2-X} NCs and annealed CeO_{2-X} powders to contrast the systems. The origin of the ferromagnetic-like ordering was determined by comparing the samples using magnetic circular dichroism (MCD) spectroscopy. It was found that the origin of d^0 ferromagnetic-like ordering in CeO_2 may be caused by charge transfer-mediated magnetism. Where a delocalized charge transfer from either electrons trapped in oxygen vacancies or O 2p valence electrons to Ce 4f mid-band gaps states causes Stoner splitting to polarize the spins at the Fermi level, creating an uneven number of unpaired spins, and an overall net magnetic moment. The magnetic ordering can be enhanced by annealing CeO_2 into bulk powders, where the magnetic signal was controlled directly by the grain size of the crystals and indirectly supported by the concentration of Ce^{3+}/oxygen vacancy defects. With further characterization using temperature dependent XRD, SEM analysis of grain sizes, additional PPMS data, and temperature dependent MCD, the room temperature ferromagnetic-like ordering in CeO_2 can ultimately be confirmed and CeO_2 could become a promising candidate material for spintronic applications.

Acknowledgements

I would like to thank my lab mates and my advisor, Prof. Pavle Radovanovic, for helping me along the way. In addition, I would like to thank Luke Menezes, Madi Donohoe, and Prof. Holger Kleinke for helping and letting me use their powder XRD instrument. Finally, I would like to thank the Canadian Centre for Electron Microscopy at McMaster University for helping me collect HRTEM data.

Table of Contents

List of Figures

List of Tables

List of Abbreviations

NC	Nanocrystal
Olam	Oleylamine
Olac	Oleic acid
LED	Light emitting diode
QLED	Quantum dot emitting diode
HOMO	Highest occupied molecular orbital
LUMO	Lowest occupied molecular orbital
eV	Electron volt
nm	Nanometre
E_g	Band gap energy
T_C	Curie temperature
T_N	Neel temperature
H_C	Coercivity
sccm	Standard cubic centimetre per minute
K	Kelvin
T	Tesla
Oe	Oersted

Chapter 1

Introduction

1.1 Dilute Magnetic Semiconductor Oxides

Dilute magnetic semiconductor oxides (DMSOs) are a class of materials that exhibit both magnetic and semiconductor properties.[1] To create a DMSO, often transition metal or lanthanide dopants are added to introduce magnetic ordering to a non-magnetic host lattice.[2] To observe intrinsic magnetic properties of a host material, approximately 1% or less dopant-host ratio is used, while to observe dopant properties approximately 10% or more dopant-host ratio is used.[3] Common examples of DMSOs are transition metal-doped ZnO, In_2O_3, SnO_2, and TiO_2.[4,5] DMSOs are of interest due to their multifunctionality and application in multiferroics and spintronics like spin light-emitting diodes and spin field-effect transistors.[6,7,8,9] However, the hardest challenge with the prior devices is needing materials that are ferromagnetic above room-temperature (RT) and have high spin-polarized carrier injection and transport.[9] DMSOs show promising potential as spin-injection contacts in these devices due to having semiconductor properties and a controllable dilute concentration of magnetic centers.[3,10,11]

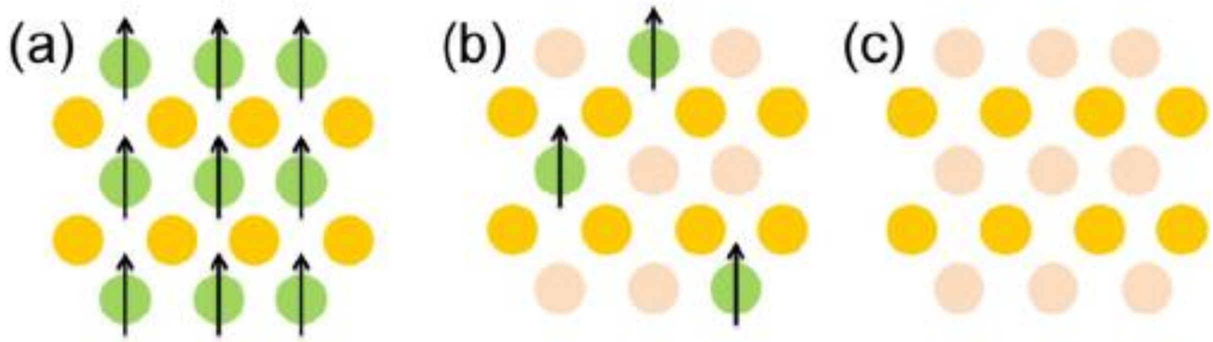

Figure 1. Different types of semiconductors: a) magnetic semiconductor, b) dilute magnetic semiconductor, and c) non-magnetic semiconductor.[9] Reprinted with permission from (Ning, S. et al. *J. Mater. Sci. Technol*. **2015**, 31. DOI: 10.1016/j.jmst.2015.08.011). Copyright (2015) Journal of Materials Science and Technology.

1.2 Types of Magnetism and Exchange Interactions

Depending on the dopant and intrinsic behaviour of the host material, different types of magnetic behaviour can be produced. Most materials are either diamagnetic or paramagnetic at room temperature.[1,6,12] Materials that are diamagnetic have all their highest occupied molecular orbital (HOMO)/valence electrons paired, and materials that are paramagnetic have unpaired HOMO electrons that are randomly orientated due to thermal disordering.[1,6,12] When the temperature is lowered below the Curie temperature (T_C for ferromagnetic, ferrimagnetic, and superparamagnetic ordering) or Neel temperature (T_N for antiferromagnetic ordering), which are unique to each material, magnetic ordering of unpaired electrons will overcome thermal disordering and the unpaired electrons will align with each other.[1,6,12]

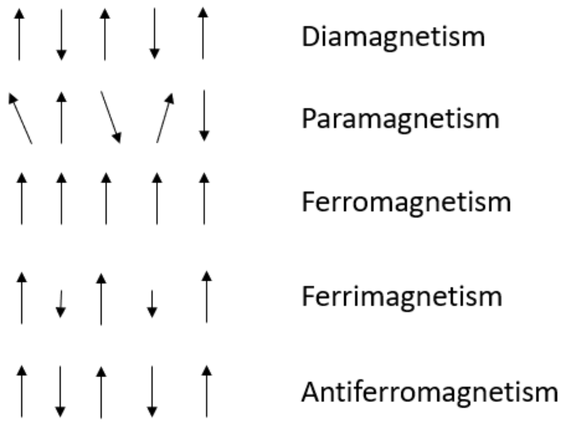

Figure 2. Different types of magnetic ordering of paired and unpaired electrons.

As shown in Figure 2, ferromagnetism is when all unpaired electrons align parallel to each other in one direction creating an overall magnetic moment and a residual magnetization.[1,6,12] Antiferromagnetism is when all unpaired electrons align antiparallel to each other and there is zero net magnetic moment.[1,6,12] For ferrimagnetism, all unpaired electrons align antiparallel but the neighbouring spins do not fully cancel each other and creates an overall net magnetic moment.[1,6,12] Finally, superparamagnetism is ultimately determined by the particle size of a nanocrystal (NC).[13] When the size of ferromagnetic NCs is reduced to a critical size, a single NC can be treated as a single magnetic domain, and its magnetic moment as a single magnetic moment.

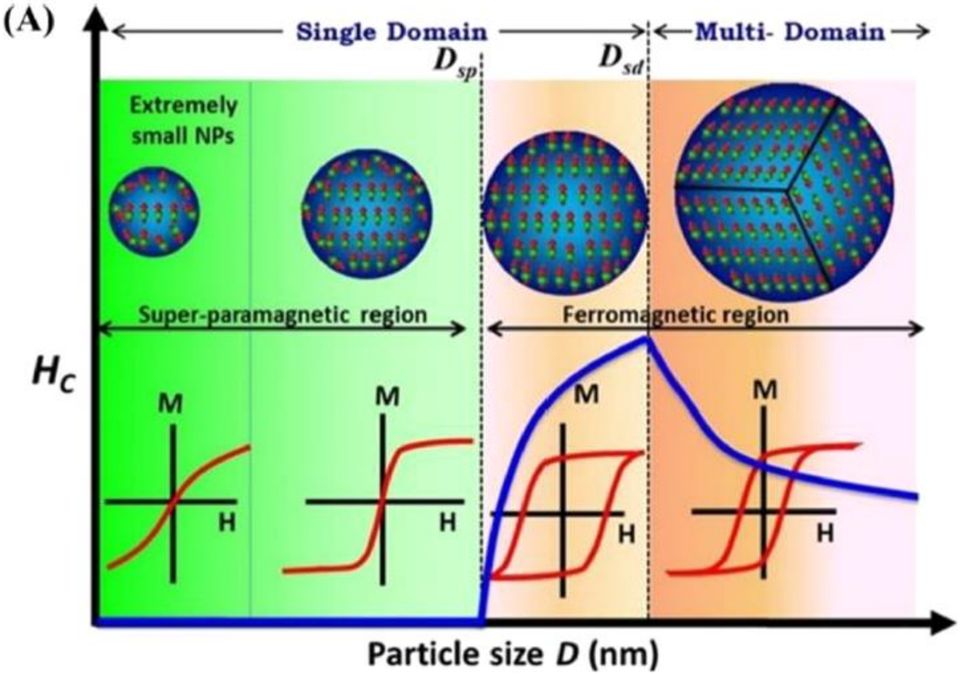

Figure 3. Magnetic hysteresis of ferromagnetic and superparamagnetic nanocrystals with various size.[13] Reprinted with permission from (Ma, Z. et al. *Chem. Rev*. **2023**, 123, 7, 3904–3943. DOI: https://doi.org/10.1021/acs.chemrev.1c00860). Copyright (2023) ACS Publications.

In bulk, magnetic properties are determined from coupling of free electrons in magnetic domains and domain-domain interactions.[13] By reducing to nano-dimensions, materials cannot support multiple domains.[13] Due to this, smaller nanocrystals behave like superspins where the entire particle has one magnetic moment that thermally fluctuates like spins in paramagnetic materials, showing no coercivity (H_C).[13] Coercivity is the ability of a ferromagnetic material to resist an external magnetic field without being demagnetized and can be measured using a hysteresis loop as shown in Figure 3.[13] So as the size of a nanocrystal decreases to a critical size, the nanocrystal will transition from being ferromagnetic (multiple domains) to superparamagnetic (single domain) and show no coercivity.[13] Although, sometimes single domain NCs can show coercivity if there is a bias to reversal of the external magnetic field caused by pinning from exchange interactions.[14]

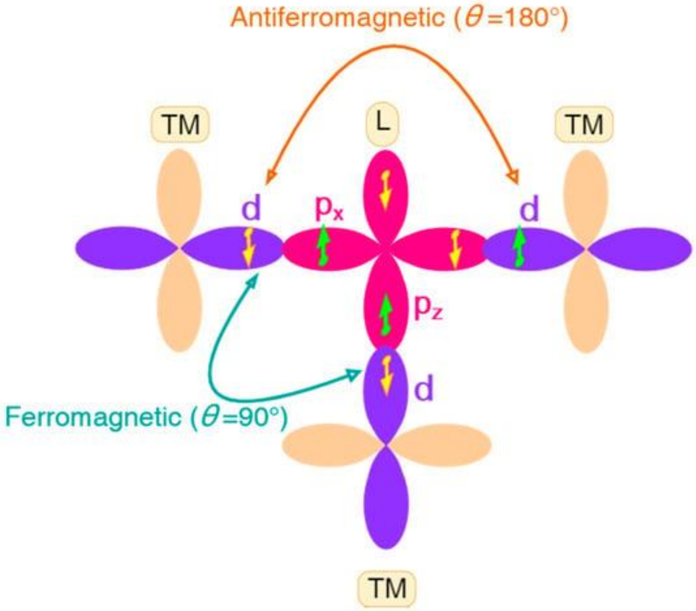

Figure 4. Diagram of ferromagnetic and antiferromagnetic superexchange interactions.[15] Reprinted with permission from (Li, X. et al. Spin Hamiltonians in Magnets: Theories and Computations. *Molecules.* **2021**, 26, 803. DOI: https://doi.org/10.3390/molecules26040803). Copyright (2021) MDPI.

The magnetic ordering of a material is determined either by direct exchange interactions or mediated exchanges, and how the coupled electrons are physically orientated in a lattice relative to each other.[15] Other factors that change the crystal structure or the position of unpaired spins will encourage different exchange interactions. The simplest exchange interactions are direct exchanges, where two magnetic species are directly in contact with each other (Ex. Ni^{2+}- Ni^{2+}) and their spins are coupled.[13,16] Meanwhile for superexchange interactions, a type of mediated exchange interaction, two magnetic species are bridged by a non-magnetic bridging ligand.[13,15] Depending on the bond angle, the magnetic ordering is either antiferromagnetic (180˚) or ferromagnetic (90˚) as shown in Figure 4. In the case with antiferromagnetism, the spins pair along one axis and there are no unpaired spins, while for ferromagnetism there are two unpaired spins on the bridging ligand due to the symmetry of the bonding.[15] Thus, the position of magnetic species and local symmetry are large factors that directly influence the type of magnetic ordering that will occur.

1.3 Properties and Magnetic Ordering in Metal Oxides

Metal oxides are a common class of semiconductors with many different applications and a wide variety of materials that can be made. For example, plasmonic metal oxide NCs ($Sn:In_2O_3$, WO_{3-X})[17,18], catalytic metal oxide NCs (CeO_{2-X})[19], or magnetic metal oxide NCs ($Co:Fe_3O_4$)[20]. In each case, the crystal structure can vary from hexagonal to cubic, but the composition always contains metal cations and oxygen anions.[21] Metal oxides are often very stable at high temperatures, can be both ionic and electronic conductors, and forming metal-oxygen bonds is energetically favourable so metal oxides are quite easy to synthesize.[21]

Common defects that occur in metal oxides are oxygen vacancies, interstitial defects, and dangling bonds.[21] When annealing metal oxides and other semiconductors, defects will migrate during annealing and move towards the surface to stabilize the core structure.[22] The surface of metal oxides NCs will have a higher concentration of defects, usually in the form of oxygen vacancies and dangling bonds.[22,23] This is because NCs are imperfect crystals that have boundaries of their long-range order and thus, there are unreacted bonds along the surface called dangling bonds.[23] These defects can also break local symmetry of nearby metal ion sites.[24] Overall, the concentration and types of defects can be controlled by changing the synthesis conditions.[21]

The origin of magnetic ordering in metal oxides varies between each system, so this makes it quite challenging to determine the correct mechanism. However, there are a few common mechanisms discussed in literature which can mediate magnetic ordering: bound magnetic polaron (BMP) theory[25], F-center exchange (FCE)[26], and charge transfer[9,27]. BMP describes how polarons, phonon clouds formed from moving electrons bound to defects in the crystal lattice, often an oxygen vacancy, overlap with neighbouring polarons to create long-range ordering.[25] Shown below in Figure 5. The degree of overlapping determines if the magnetic ordering is either ferromagnetic (lots of overlap) or ferrimagnetic coupling (little overlap), while an isolated polaron is treated as a paramagnetic site.[25]

FCE is a subset of BMP that describes how point defects at anion sites in a lattice, which are called F-centers, couple to neighbouring magnetic ions with unpaired electrons or other F-centers.[26,28] In the case with metal oxides, F-centers would always be different types of oxygen vacancies.[26,28] When an oxygen vacancy is formed, conduction electrons can be trapped in localized states after relaxing from the conduction band preventing exciton recombination.[29] These trapped electrons can then couple to nearby magnetic ions, and depending on the distance the interaction can be a direct exchange interaction. Lastly, charge transfer-mediated approach describes how a local charge reservoir either a cation existing in two different oxidation states, or a charge-transfer complex occurring on the surface, then electron transfer is able to increase the Fermi level to a peak in the local density states causing Stoner splitting of your density of states.[4,27,30] To note, Stoner splitting is the spin polarization of the density of states into an uneven number of up or down spins, creating a net magnetic moment.[27]

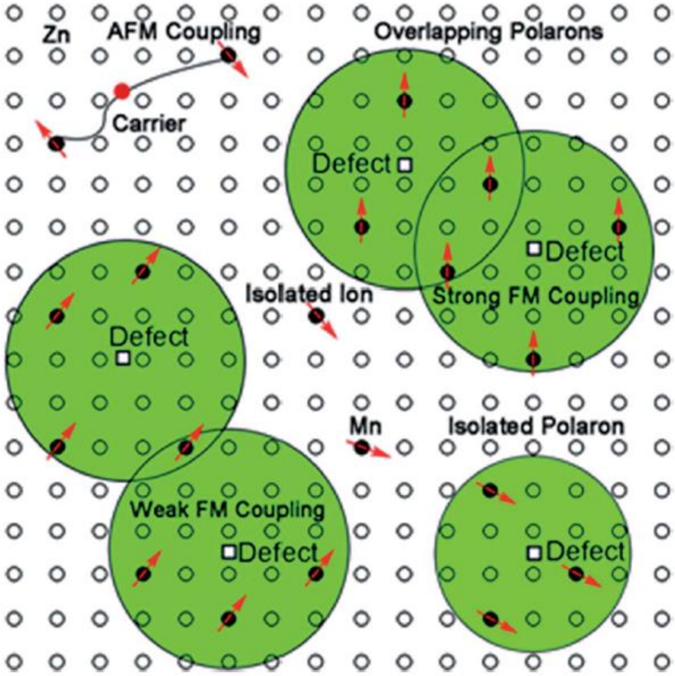

Figure 5. Potential mechanism of magnetic ordering in metal oxide nanocrystals.[25] Reprinted with permission from (F. L. Tang. et al. *RSC Adv*. **2014**, 4, 49308-49314). Copyright (2018) American Physical Society.

1.4 d^0 Magnetism

d^0 magnetism is an unexplained magnetic behaviour found in traditionally diamagnetic materials that do not follow Curie-type behaviour.[9,31,32] Typically, d^0 magnetic samples show an S-shape saturation curve that is temperature independent and shows no hysteresis like in Figure 6., excluding ferromagnetic or superparamagnetic ordering to cause this effect.[33] Thus, depending on the sample d^0 materials show ferromagnetic or antiferromagnetic-like behaviour.[33] This behaviour is also found in several undoped DMSOs like ZnO and CeO_2.[31–34] Determining the mechanism of d^0 magnetism is still a challenge as plenty of experimental data has been collected but multiple conflicting theories have been proposed in the literature.[26,27,33,34]

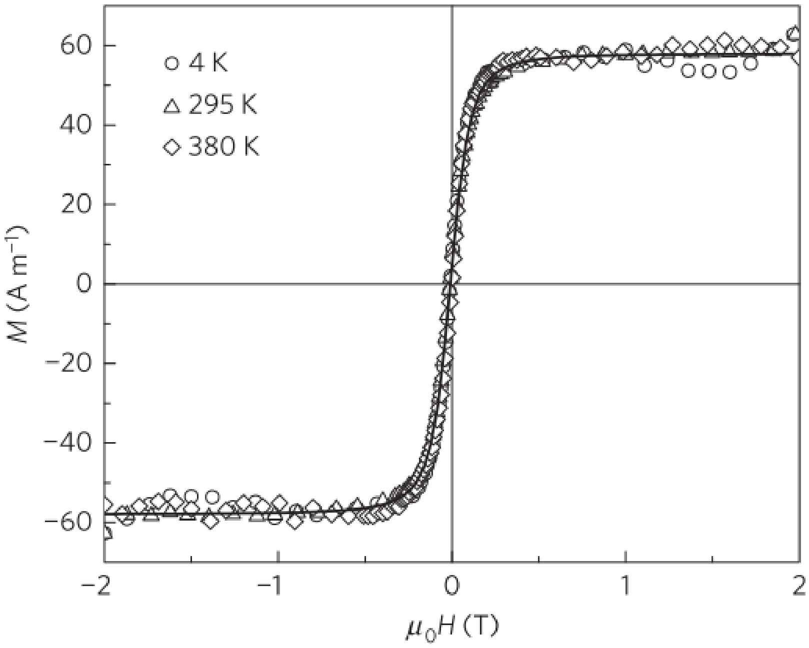

Figure 6. Magnetization curves of 4 nm CeO_2 nanocrystals (4 mg) at 4 K, 295 K and 380 K.[33] Reprinted with permission from (Coey, M. et al. *Nat. Phys*. **2016**, 12, 694–699. DOI: doi.org/10.1038/nphys3676). Copyright (2016) Springer Nature.

1.5 Electronic and Crystal Structure of CeO_2

CeO_2 is a wide band gap semiconductor (~3.5 eV for its first transition and ~5.5 eV for its section transition) with cubic fluorite structure ($Fm\bar{3}m$).[34,35] Its colour ranges from pale yellow-white to blue/black depending on the oxygen stoichiometry.[36] When in a very oxygen rich environment the colour is a pale-yellow white, and blue/black in a very oxygen deficient environment.[36] The change in colour from almost white to black is also observed in TiO_2.[37]

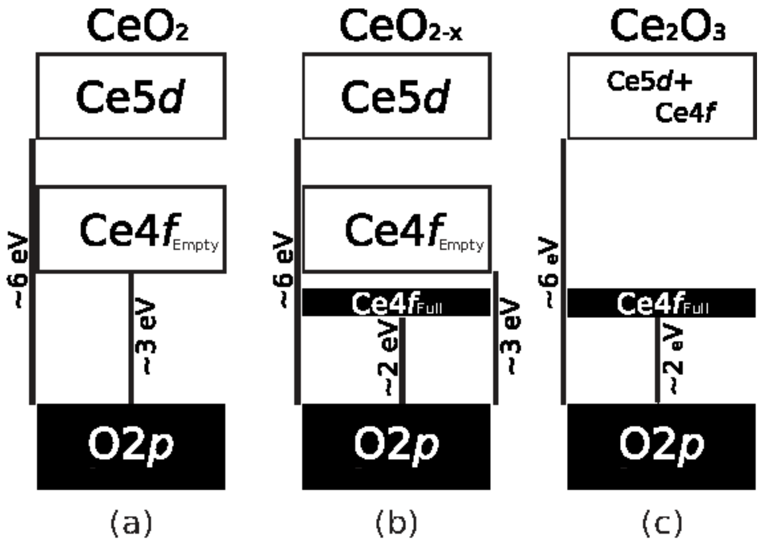

Figure 7. Theoretical B3LYP calculations of CeO_2 electronic structure.[35] Reprinted with permission from (Kullgren, J. et al. *J. Chem. Phys*. **2010**, 132, 054110). Copyright (2010) AIP Publishing.

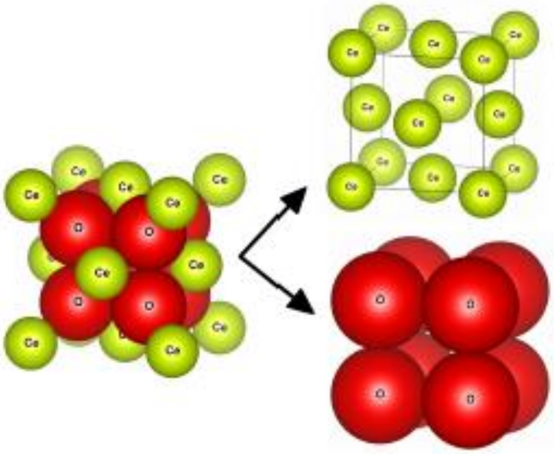

Figure 8. Crystal structure of CeO_2.[34] Reprinted with Permission from (Paidi, V.K. et al. *Phys. Rev. B*. **2018**, 99, 180403(R)). Copyright (2018) American Physical Society.

CeO_2 has an ability to reversibly convert between Ce^{4+} and Ce^{3+} oxidation states.[34,38] This is caused by the small stability difference between lanthanides preferring Ln^{3+} oxidation state and noble gas configuration.[38] For most lanthanides, they prefer the Ln^{3+} oxidation state due to the removal of the 6s electrons and one 4f electron, removing anymore electrons from the 4f orbital requires a tremendous amount of energy.[38,39] The high energy to remove additional electrons from the 4f orbital is due to the 4f orbital penetrating closest to the nucleus, and thus being very stable.[40] Except, cerium is an exception to this pattern due to having only one 4f electron in the ground state (Ce, $[Xe]4f^15d^16s^2$).[40] In the ground state, both Ce^{4+} and Ce^{3+} are present but the Ce^{4+} is more abundant, and this is because Ce^{4+} has noble gas configuration which is slightly more stable.[38,40] Due to both Ce^{4+}/Ce^{3+} oxidations states being present in the ground state, even if CeO_2 is ideally made, in reality there will always be a degree of non-stoichiometry so the band structure will resemble CeO_{2-X} where the Ce 4f mid band gap states are partially occupied.[35]

1.6 Properties of CeO_2

Due to the relative energy difference between the Ce^{3+}/Ce^{4+} oxidation states, Ce can reversibly convert between the two states which results in CeO_2 having excellent catalytic properties.[41] For example, CeO_2 powder is used in catalytic converters of cars for the oxidation of CO.[36,41,42]

$$2\,CeO_2 + CO \rightarrow Ce_2O_3 + CO_2 \quad (Lack\ of\ O2)$$

$$2\,Ce_2O_3 + O_2 \rightarrow 4\,CeO_2 \quad (Excess\ O_2)$$

Where in an oxygen lacking atmosphere, CeO_2 is reduced to Ce_2O_3 and CO is oxidized to CO_2. While in an ambient atmosphere Ce_2O_3 is oxidizes back to CeO_2 overtime, since Ce_2O_3 is only metastable.[36,40–42]

CeO_2 can also have either ionic (0.1 S/cm, p-type, buk) or electronic ($1x10^{-7}$ S/cm, nano, n-type) conductivity, but the type of conductivity depends on the grain size of the particles.[43,44] At lower grain sizes, particles have a higher surface-to-core ratio so the conductivity is mostly caused by the mobility of surface electrons.[43,44] However as the grain size increases, the conductivity switches from n-type to p-type as the mobility of oxygen and oxygen vacancies dominates and core effects overwhelm surface effects due to having a smaller surface-to-core ratio as seen below in Figure 10.[43,44]

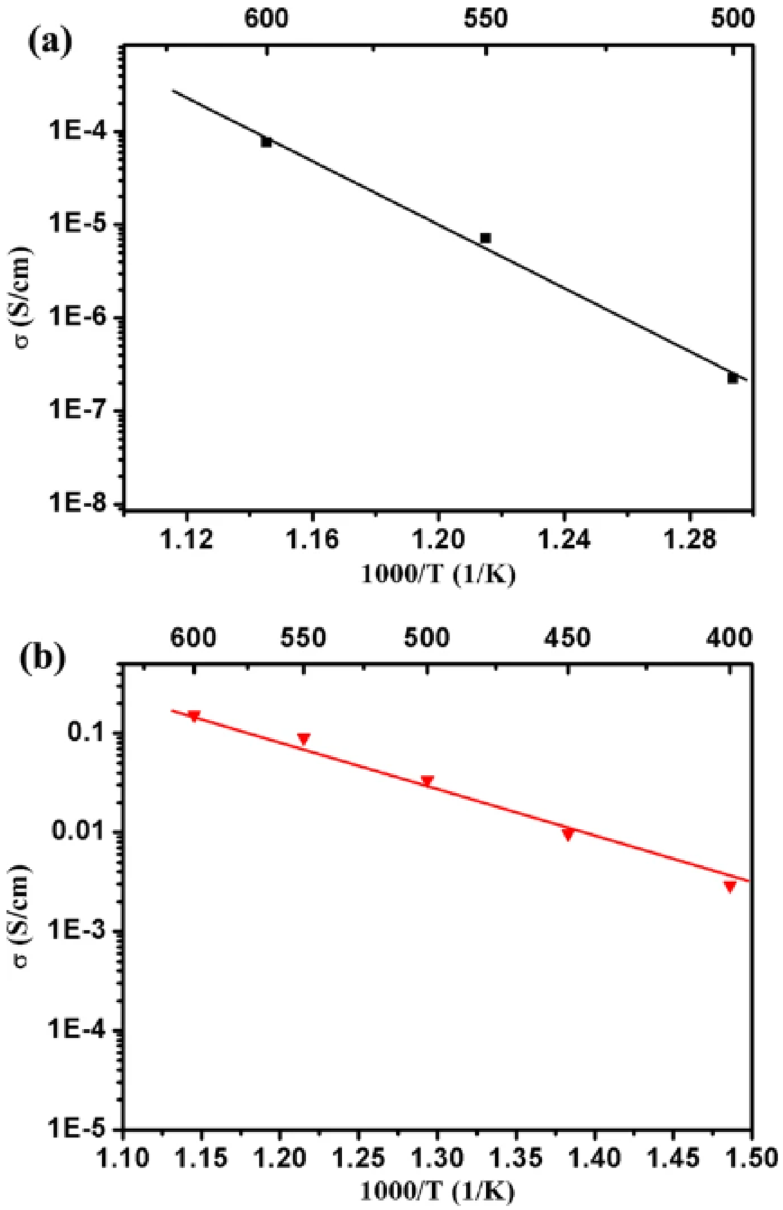

Figure 9. Grain boundary conductivity of CeO_2 as a function of temperature obtained in (a) air and (b) H_2/air atmospheres.[43] Reprinted with permission from (Wang, B. et al. *NPG Asia Mater*. **2019**, 11(51). DOI: 10.1038/s41427-019-0152-8). Copyright (2019) Springer Nature.

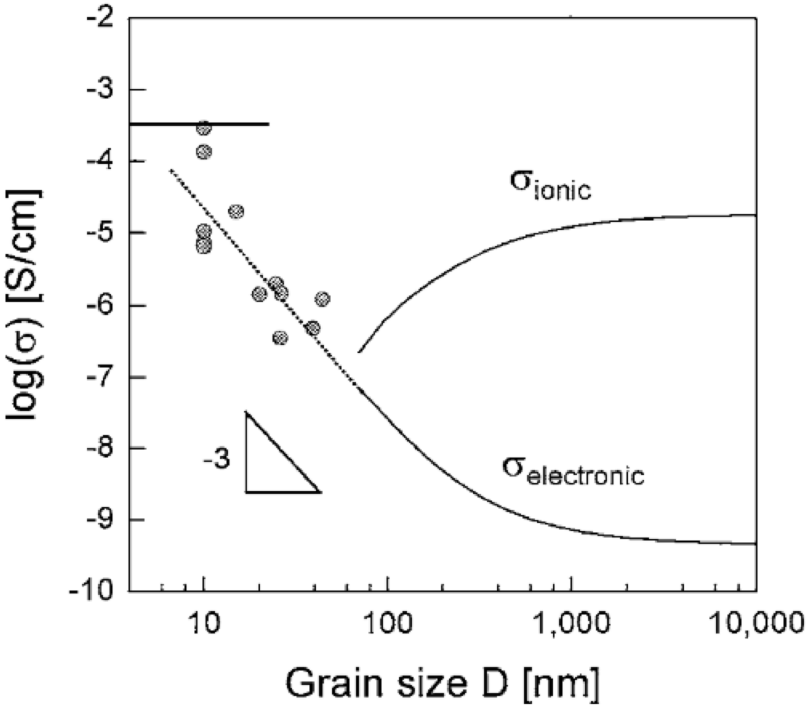

Figure 10. Electrical conductivity of CeO_2 as function of grain size.[44] Reprinted with permission from (Tschöpe, A. et al. *J. Electroceramics*. **2001**, **7**, 169–177). Copyright (2001) Kluwer Academic Publishers.

1.7 Magnetic Ordering in CeO_2

It has been observed that CeO_2 shows a room-temperature ferromagnetic-like behaviour that is similarly found in other d^0 magnetic materials.[33] Multiple theories have been proposed for the origin of this magnetic ordering such as BMP theory[34], clustering of Ce^{3+} and vacancy defects[3,26], giant orbital paramagnetism[33], and charge transfer[27]. Shown in Figure 11., the ferromagnetic-like response is enhanced when CeO_2 is doped with a non-magnetic ions like La^{3+}, but is later quenched by dispersing the powder over 100 nm.[32] The addition of dopants is known to increase the concentration of Ce^{3+} defects in the lattice but the magnetic ordering is also distance dependent.[45] So it appears that the concentration of defects do play a role in the ferromagnetic-like ordering but the direct impact of these defects is unknown, and considering the presence of charge transfer from the O 2p valence band to Ce 4f mid band states, the mechanism likely has multiple components.[34]

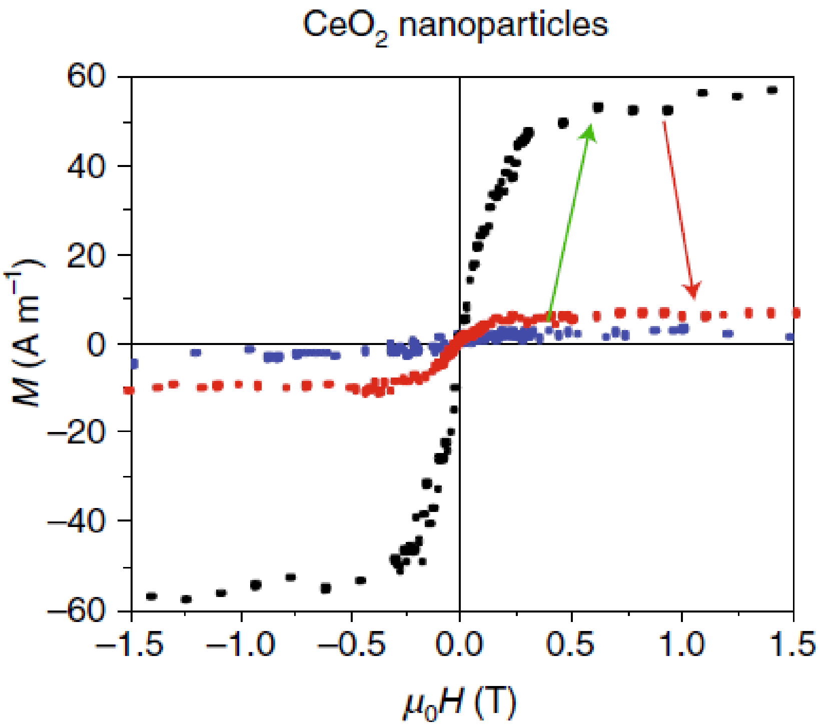

Figure 11. d^0 magnetism induced in CeO_2 nanocrystals (3 nm) via doping with non-magnetic La^{3+} and quenched by dispersing over 100 nm with non-magnetic filler γAl_2O_3.[32] Reprinted with permission from (Coey, J.M.D. *Nat. Mat*. **2019**, 18, 652–656. DOI: 10.1038/s41563-019-0365-9). Copyright (2019) Springer Nature.

1.8 Motivation and Scope of Thesis

The objective of this thesis was to study the magnetic properties of undoped CeO_2 to determine the mechanism causing the room-temperature ferromagnetic-like behaviour. This was done by systematically annealing undoped CeO_2 from nanocrystals into bulk powders under different annealing time, temperature, and atmosphere to observe grain size and defect concentration impacts on the magnetic ordering. Structural characterization, optical, magnetic, and magneto-optical measurements were then conduct on colloidal CeO_{2-X} nanocrystals (NC) and annealed CeO_{2-X} powders to contrast the systems. Different types of magnetic measurements were obtained using a physical property measurement system (PPMS) and then compared with magnetic circular dichroism spectroscopy (MCD) measurements to find which optical transition and species is causing the ferromagnetic-like ordering in CeO_2.

In Chapter 2, the experimental methods and sample preparations are described. Colloidal CeO_{2-X} NCs were synthesized at 325˚C for 2 hr under N_2 flow using the heat up approach and annealed CeO_{2-X} powders were made from annealing the colloidal NCs under different conditions. Powder X-ray diffraction (XRD), high resolution transmission electron microscopy (HRTEM), energy dispersive X-ray spectroscopy (EDS), UV-vis-NIR absorption spectroscopy, magnetization measurements (PPMS), and magnetic circular dichroism (MCD) spectroscopy were utilized to fully analyze the samples.

In Chapter 3, colloidal quantum dot CeO_{2-X} NCs synthesized at 250˚C, 275˚C, 300˚C, and 325˚C were compared. It was found that the intensity of the two absorption peaks at 281 nm and 231 nm were inversely proportional to temperature. With synthesis temperatures above 300˚C the 281 nm peak was higher in intensity, while with synthesis temperatures below 275˚C the 231 nm peak was more pronounced. Additionally, the particle size increased and the XRD peaks narrowed with increasing temperature. Lastly, colloidal 325˚C NCs were studied using MCD spectroscopy. In the end, several broad overlapping likely C-term peaks with S=0.5 were observed and were later compared to the annealed powders to identify the transitions.

In Chapter 4, the synthesized CeO_{2-X} NCs were annealed to compare the effects of annealing time, temperature, and atmosphere on the ferromagnetic-like behaviour. It was found that annealing for 24 hours at 600˚C in air was the ideal time and temperature to get the highest ferromagnetic-like signal. Above 24 hr and 600˚C, the magnetic saturation of the samples decreased as more vacancies were filled in, evident with the sample colour changing from pale yellow to white. Although it was found that the concentration of Ce^{3+}/oxygen vacancy defects only played an indirect role in enhancing the ferromagnetic-like component of the magnetic signal. While the ferromagnetic-like ordering was mainly controlled by the crystal grain size of the powders. Finally, MCD spectroscopy was used to compare air and H_2/N_2 atmosphere annealed CeO_{2-X}. For the 24 hr 600˚C air annealed sample, the origin of the ferromagnetic-like ordering was associated with a delocalized charge transfer occurring from either trapped electrons in oxygen vacancies or O 2p valence electrons to the Ce 4f (unoccupied) mid-band gap states.

In Chapter 5, I summarize the results reported throughout this thesis and give an outlook on the future research directions and prospects of this work. I suggest that the origin of the d^0 ferromagnetic-like ordering in undoped CeO_2 is caused by charge transfer-mediated magnetism. Where a delocalized charge transfer occurs from either electrons trapped in oxygen vacancies or O 2p valence electrons to Ce 4f mid-band gaps states causes Stoner splitting to polarize the spins at the Fermi level, creating an uneven number of unpaired spins, and an overall net magnetic moment. The magnetic ordering can be enhanced by annealing CeO_2 into bulk powders, where the magnetic signal is controlled directly by the grain size of the crystals and indirectly supported by the concentration of Ce^{3+}/oxygen vacancy defects. With further characterization using temperature dependent XRD, SEM analysis of grain sizes, additional PPMS data, and temperature dependent MCD, the room temperature ferromagnetic-like behaviour in CeO_2 can ultimately be confirmed and CeO_2 could become a promising candidate material for spintronic applications.

Chapter 2

Experimental Section

2.1 Materials

Cerium(III) acetylacetonate dihydrate (Ce(acac)$_3$·2 H_2O, 99.9%) was purchased from Strem Chemicals. Oleic acid (Olac, 90%) was purchased from Alfa Aesar. Ethanol (reagent grade), acetone (≥ 99.5%), hexane (95% anhydrous), and oleylamine (Olam, 70%) were purchased from Sigma-Aldrich. All chemicals were used as received without further purification.

2.2 Synthesis and Sample Preparation

2.2.1 Synthesis of Colloidal CeO_{2-X} NCs

Colloidal CeO_{2-X} NCs were synthesized using a modified colloidal synthesis method. In a typical synthesis of CeO_{2-X} NCs, 0.2 g (0.4 mmol) of Ce(acac)$_3$·2 H_2O is dissolved in a mixture of 4 g (15.0 mmol) of Olam and 2 g (7.1 mmol) of Olac in a three-neck flask while stirring[46–48]. The solution is slowly heated to the reaction temperature (Ex. 325 °C) and left to react for 2 hours under nitrogen flow. The reaction mixture is then cooled down to 100 °C with a heat gun. Due to the high viscosity of the mixture, 10 mL of ethanol is added to the mixture to ease transferring to a centrifuge tube. Afterwards, 5 mL of ethanol is added for a total mixture volume of approximately 15-20 mL (257.2 – 342.9 mmol). The exact amount of antisolvent is not crucial if it is in excess to the reaction mixture. Depending on the reaction temperature, immediate precipitation of the product might be observed after adding antisolvent. The mixture is cycloned and then centrifuged at 7830 rpm for 10 minutes. After centrifuging, a dark red-amber precipitate and a dark orange-yellow translucent liquid layer will be present. If the liquid layer is still opaque, it can be further diluted with excess ethanol or acetone and recentrifuged to collect more product. The liquid layer is then decanted, and the precipitate is collected. The precipitate is redispersed in 15 mL of hexane (114.8 mmol) and the final solution varies from a dark translucent red amber to yellow amber colour depending on the reaction temperature. The final product can be readily dispersed in most non-polar solvents. Due to the nature of CeO_{2-X}, a degassing step or dehydrating the precursors was not necessary to obtain the final product. While degassing can create more oxygen vacancies, the CeO_{2-X} NCs were always non-stoichiometric without degassing due to the presence of Ce^{3+} defects naturally forming in the ground state.

2.2.2 Annealed CeO_{2-X}

Annealed CeO_{2-X} powders were prepared using previously made CeO_{2-X} NCs. Colloidal NC solutions were added to a ceramic crucible that was cleaned prior using dilute nitric acid. Once the solution was added, a heat gun was used to evaporate the solvent, leaving behind only the CeO_{2-X} precipitate. The crucible was then inserted into a furnace (Vulcan A-130 100/120V) and heated at various temperatures (400°C, 600°C, 800°C, and 1000°C). Once at the annealing temperature the NCs were left to anneal in ambient air for various lengths of time (1 hr, 8 hr, 24 hr, and 48 hr). When finished, the furnace was turned off and the samples were left to slowly cool to room temperature overnight. For the time annealed series, a single sample was annealed cumulatively up to 48 hr to control only for annealing time. And for the temperature annealed series, a batch of sister samples were prepared and annealed at different temperatures with the same annealing time to control for annealing temperature while minimizing the deviation in defect concentration per sample. For the atmosphere annealed series, the sample was prepared by annealing CeO_{2-X} NCs in our chemical vapour deposition furnace (Atomate chemical vapour deposition furnace controlled by an Intellisys adaptive pressure controller) under H_2/N_2 (containing 5% H_2) flow at 50 sccm for 24 hr at 600°C. After the annealing, the sample was left to slowly cool like the air annealed samples.

2.3 Measurement and Data Analysis

2.3.1 Powder X-ray Diffraction

Powder X-ray diffraction (XRD) measurements were performed using an INEL XRD diffractometer from Dr. Holger Kleinke’s group in the Department of Chemistry at the University of Waterloo. The diffractometer is equipped with a position-sensitive detector that utilizes monochromatic Cu-Kα radiation ($\lambda = 1.5406$ Å). The lattice parameter and crystalline size were estimated using the Debye-Scherrer equation:

$$T = \frac{C\lambda}{B\cos\theta} \quad \text{(Equation 2.1)}$$

where T is the crystallite thickness, C is a dimensionless shape factor with a value close to 1, λ is the wavelength of the X-rays used (1.54 Å), θ is the diffraction angle in radians, and B is the full width at half maximum (FWHM). XRD samples were prepared by either drop-casting colloidal suspensions of NCs onto a silicon substrate or packing dried powders onto an aluminum substrate.

2.3.2 Transmission Electron Microscopy and Energy Dispersive X-ray Spectroscopy

High resolution transmission electron microscopy (HRTEM) samples were prepared via depositing diluted colloidal suspensions of NCs onto copper grids with lacey Formvar/carbon support films purchased from Ted Pella, Inc. HRTEM imaging and energy dispersive X-ray spectroscopy (EDS) elemental analysis were performed with a Talos 200X operated between 80 and 200 kV, and equipped with four in-column SDD Super-X detectors from the Canadian Centre for Electron Microscopy at McMaster University.

2.3.3 UV-vis-NIR Absorption Spectroscopy

Optical absorption spectra were obtained using a Varian Cary 5000 UV-Vis-NIR spectrophotometer in the range of 200 nm to 3300 nm. Measurements of diluted colloidal suspensions were collected using 1 X 1 cm wide quartz cuvettes and a reference solvent. For collecting absorption data to compare with MCD data, diluted CeO_{2-X} NC solutions were drop-casted onto strain-free quartz substrates, and solid samples were annealed while on the substrates.

2.3.4 Magnetization Measurements

Magnetization measurements were obtained using a Physical Property Measurement System (PPMS) Quantum Design Model 6000. PPMS samples were prepared by grinding annealed samples into fine powders using a mortar and pestle then loaded into gelatin capsules. Saturation measurements were collected at 2 K from 0 to 9 T. Zero field cooling/field cooling (ZFC/FC) measurements were performed from 300 K to 2 K at 1500 Oe. Finally, magnetic sweep measurements were conducted from 1 to -1 T at 2 K, 10 K, and 300 K.

2.3.5 Magnetic Circular Dichroism Spectroscopy

Magnetic circular dichroism (MCD) spectroscopy is a magneto-optical technique that measures the difference in absorption of left and right circularly polarized light.[49] MCD intensity for a transition from a ground state $|A\rangle$ to an excited state $|J\rangle$ is defined below as,

$$\frac{\Delta A}{E} = \left(\frac{2N_0\pi^3\alpha^2Cl\,log(e)}{250hcn}\right)\mu_B B\left[A_1\left(-\frac{\partial f(E)}{\partial E}\right)+\left(B_0+\frac{C_0}{kT}\right)\right]f(E) \quad \text{(Equation 2.2)}$$

where ΔA is the differential absorption between left and right circularly polarized light, $E = h\nu$, α is the electric permeability, C is the concentration, l is the path length, n is the index of refraction, μ_B is the Bohr magneton, and B is the applied magnetic field.[49] Next, A_1, B_0, and C_0 are known as the MCD A-, B-, and C-term, respectively.[49] $f(E)$ is the absorption spectrum band shape, and $\partial f(E)/\partial E$ is the first derivative.[49] Under an external magnetic field along the propagation of light in the z direction, the ground or excited states are split due to Zeeman perturbation with a magnitude of $-\mu_z B = \mu_B(g_L\hat{L}_z + g_S\hat{S}_z)B$, where $\hat{L}_z$ and $\hat{S}_z$ are the orbital and spin angular momentum operators, respectively, and $g_L = 1$ and $g_S = 2.002$ are the according gyromagnetic ratios.[49] The overall electron angular momentum responsible for the electron polarization is $J = L + S$, with the MCD selection rule $\Delta M_J = \pm 1$ (+1 for left and -1 for right circularly polarized light).[49]

A-term MCD occurs in a system that has degenerate excited states. Under magnetic field, the excited states are split due to the Zeeman effect, and since the Zeeman splitting is normally only a few wavenumbers, two oppositely signed absorption bands will average into a derivative shape MCD signal, as shown in Figure 12.[49] In the opposite case, C-term MCD requires degenerate ground states that undergo Zeeman splitting in the presence of an external magnetic field.[49] At low temperatures, the kT component is similar to or smaller than the magnitude of the Zeeman splitting in the presence of a strong magnetic field, affecting the Boltzmann population of the lower ground state sublevels to be larger than of the higher-energy sublevels.[49] Hence, two oppositely signed absorption bands will have different intensities, resulting in a single parity absorption band shape like shown in Figure 12.[49] In general, C-term MCD is associated with the Zeeman splitting caused by ground state paramagnetism, and thus follows temperature dependence attributed to Curie law.[49] To note, C-term signals are usually observed in MCD spectra of diluted magnetic semiconductors which is relevant to CeO_{2-X} which is discussed in this thesis.[49,50]

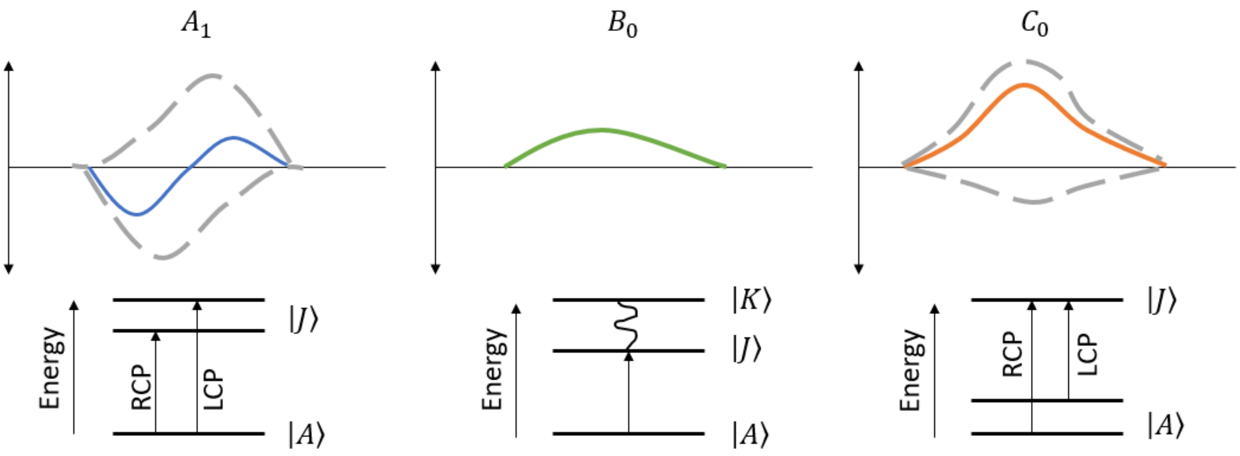

Figure 12. Diagram of MCD terms with MCD signal (top) and Zeeman splitting (bottom) for A-term, B-term, and C-term MCD.

Lastly, B-term is caused by the field-induced mixing of states. The energetic proximity of a third state $|K\rangle$ to either the excited state $|J\rangle$ or ground state $|A\rangle$ gives noticeable Zeeman coupling. As the intensity of the magnetic field increases, the amount of mixing increases to result in an absorption band shape. Like A-term, B-term is often temperature independent. So temperature dependent intensity of B-term signals can sometimes be observed when $|K\rangle$ is noticeably low-lying in energy.

MCD measurements were carried out in Faraday configuration using a Jasco J-815 spectropolarimeter for generating circularly polarized light and signal detection. Samples were held in an Oxford SM 4000 magneto-optical cryostat that allows for variable temperature (300 K to 1.5 K) and variable field (0 to 7 T) operation. The direction of the magnetic can also be switched to the opposite direction, allowing for operation between -1 to 1 T. Samples were prepared by drop casting samples onto a strain free quartz substrate, and loaded into the cryogenic chamber. The samples were cooled from then cooled from 300 K to 5 K using liquid nitrogen and liquid helium. For sample preparation, colloidal nanocrystal solutions were first drop casted onto substrates, and for annealed samples were then annealed at either 600°C for 24 hr in air or 600°C for 1 hr in H_2/N_2. Field dependence measurements were done on all samples by sweeping the magnetic field from 0 T to 7 T at 5 K. Additionally for the annealed samples, the magnetic field was swept from 1 to -1 T at 5 K to compare with the PPMS measurements that were obtained at 2 K between -1 to 1 T. The MCD intensity is expressed as ellipticity (θ, millidegrees of the transmitted light.

For analyzing the field dependence data, first baseline subtraction using the spectrum collected at 5 K 0 T was used to get high resolution MCD intensity absorption spectra. Then the corrected spectra at their MCD band maxima were plotted with respect to magnetic field (B). To extract values such as carrier population (N), Landé factor (g), or spin (S), the plotted curves were fitted using the spin-only Brillouin function,

$$M_S = \frac{1}{2} N g_S \mu_B \left[(2S+1) coth\left((2S+1)\frac{g_S \mu_B B}{2k_B T} \right) - coth\left(\frac{g_S \mu_B B}{2k_B T} \right) \right] \qquad \text{(Equation 2.3)}$$

where S is the spin quantum number, g_S is the corresponding Landé g-factor, B is the external magnetic field, μ_B is the Bohr magneton, k_B is the Boltzmann constant, and T is the temperature.[49] During the fitting N was free floated, and S and g were locked. The Brillouin function was also used to fit the magnetic saturation curves obtained using PPMS.

The circular polarization of light is defined according to the convention used in optics, referenced to the detector or facing the light source.[49] MCD intensity is defined as $\Delta A = A_L - A_R$, where A_L and A_R are the absorption of right (ρ^+) and left (ρ^-) circularly polarized light and presented as a degree of ellipticity (θ).[49] MCD intensities were then converted to $\Delta A/A$ from ellipticity using the relationship,

$$\frac{\Delta A}{A} = \frac{\theta}{32982 \times A} \qquad \text{(Equation 2.4)}$$

where θ is in millidegree and A is the absorbance from the absorption spectrum simultaneously collected by the CD detector.[49]

Chapter 3

Electronic Structure of CeO_{2-X} Nanocrystals

3.1 Appearance and Structural Characterization CeO_{2-X} Nanocrystals

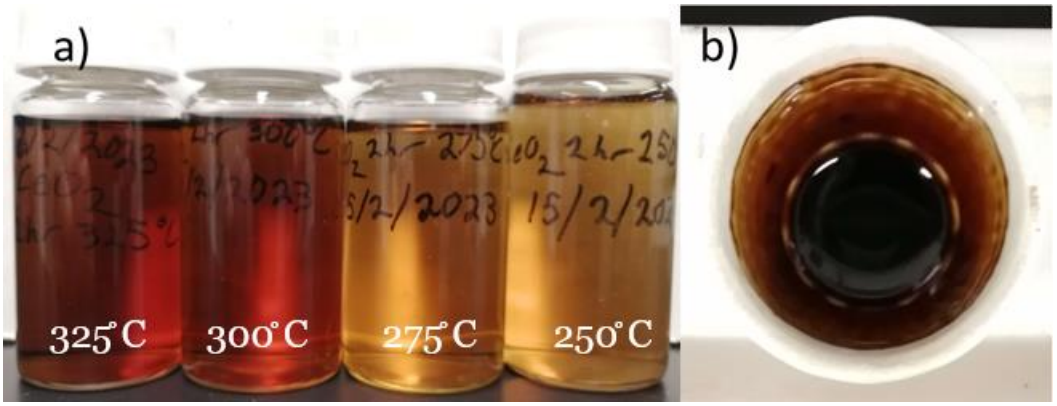

Figure 13. Physical appearance of a) CeO_{2-X} NCs colloidally dispersed in hexane and b) precipitated CeO_{2-X} NCs.

Colloidal CeO_{2-x} nanocrystals (NCs) were synthesized using the heat up approach and refluxed for two hours under inert atmosphere at the following temperatures: 250℃, 275℃, 300℃, and 325℃. All samples were translucent and colloidally stable in non-polar solvents like hexane. Shown in Figure 13., it was observed for samples made below 275℃ the colour of the solutions were a yellow amber, while for samples made above 300℃ the colour was a red amber. Regardless of which temperature, once precipitated out of solution the samples became a dark red amber sludge. The appearance of the precipitate is likely due to the very high ratio of ligands to precursor used during synthesis, with 37.5 times Olam and 17.8 times of Olac in mmols to $Ce(acac)_3 \cdot 2\ H_2O$. The yellow/red amber colour present while dispersed in solution is likely caused by sub-band gap states, and the darker shade at higher temperature is likely from having larger NCs. Conventionally as a bulk powder, CeO_2 can range from pale yellow to white depending on the oxygen stoichiometry, white being very oxygen rich and pale yellow being oxygen poor. Based on the colour this suggests the samples are oxygen poor and non-stoichiometric, and for the rest of this thesis will be labelled as CeO_{2-X} (where x is the oxygen stichometry).

In Figure 14., XRD was collected for all samples, the XRD peaks were very broad with low intensity. This implied the NCs were very small since broadening is expected for very small NCs due to lack of long-range order. It was noticeable that with increasing synthesis temperature, the NCs XRD peaks began to narrow, and at 325℃ the sample matched the cubic CeO_2 (cerianite, cubic fluorite structure, $Fm\bar{3}m$) reference pattern in Figure 15. Considering the material, only Ce_2O_3 or CeO_2 would be possible crystal structures, but because Ce_2O_3 is not stable, the CeO_2 phase is likely to form.[51] Due note, around 20° there is a small broad peak in each of the patterns, this peak is caused by the XRD instrument and substrate, which usually has increasing intensity up to 20°. This background noise is only noticeable due to the low intensity from the samples.

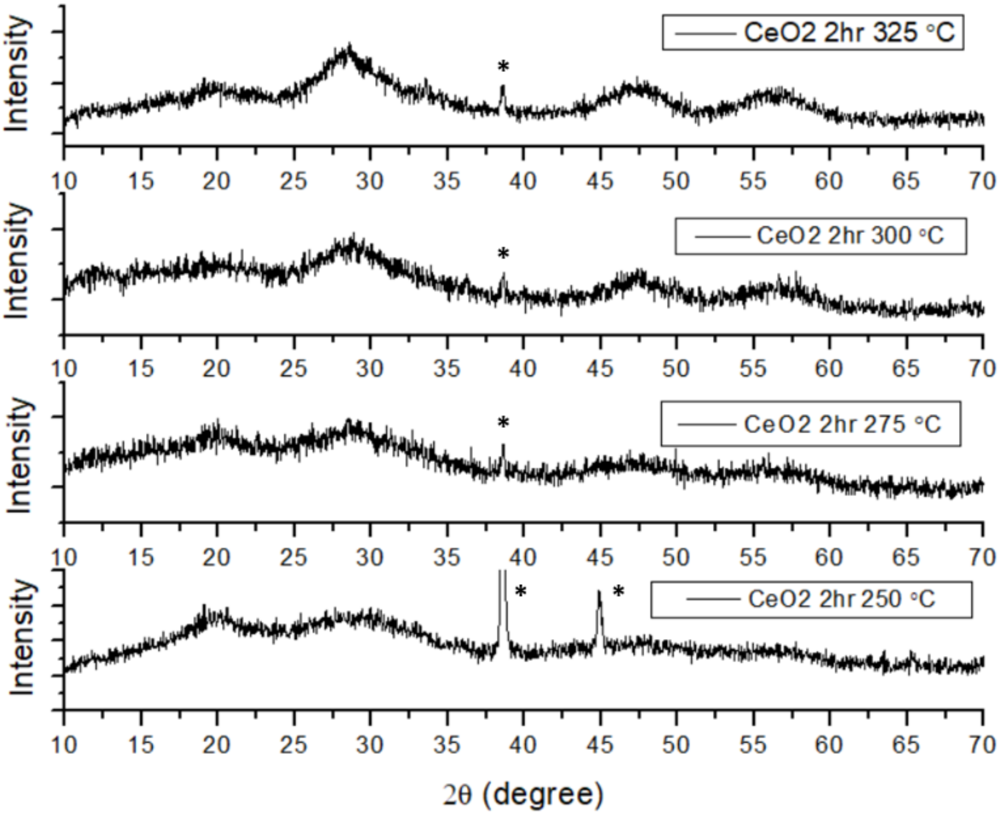

Figure 14. XRD peaks of colloidal CeO_{2-X} NCs synthesized at different reaction temperatures. Aluminum/Si substrate peaks are labeled with an asterisk (*).

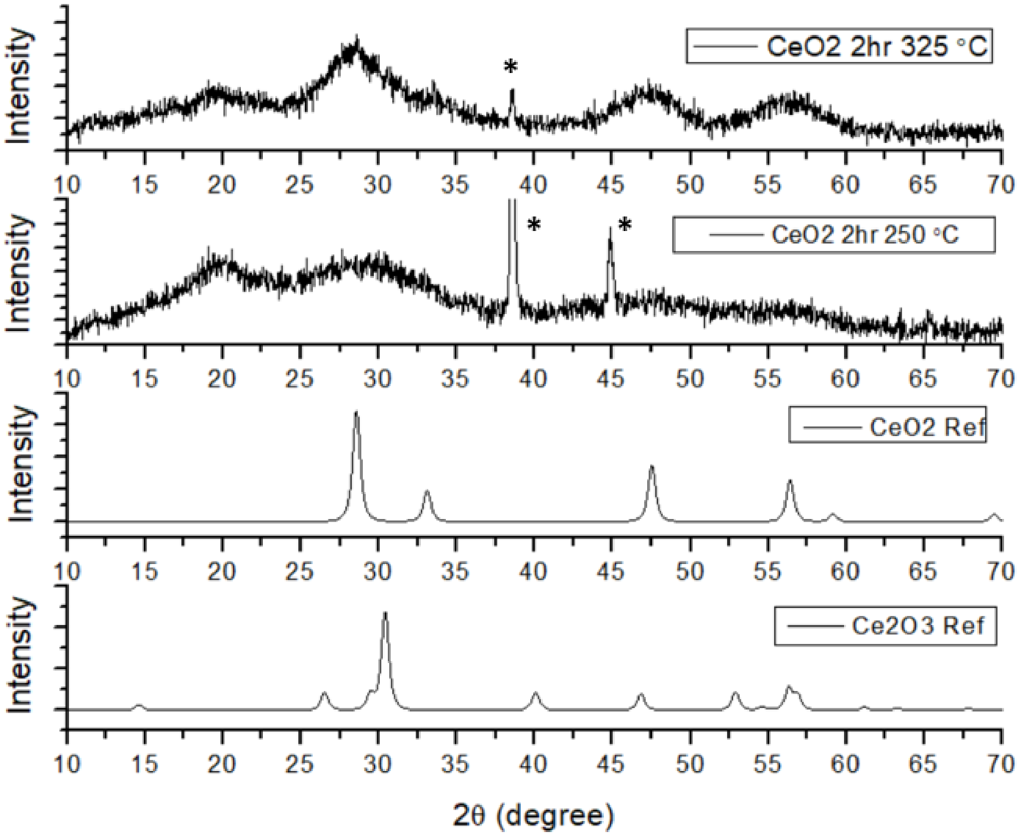

Figure 15. XRD of colloidal CeO_{2-X} NCs compared to references. The peaks at 38.49° and 44.65° are from the aluminum substrate.

The following peaks and corresponding planes observed are 28.39° (111), 33.20° (200), 47.50° (202), 56.54° (311), and 59.27° (222). However, because of the large broadening, the (111) and (200) peaks were convoluted, along with (311) and (222). Again, this is likely just due to the large broadening caused by the small particle size. With decreasing long-range order, there is less constructive interference measured from diffracted X-rays, and this is because there are fewer crystal planes for incident X-rays to deflect away from and simply pass through, so more destructive interference is recorded. Additionally, it was not possible to use the Scherrer equation to calculate the particle sizes.

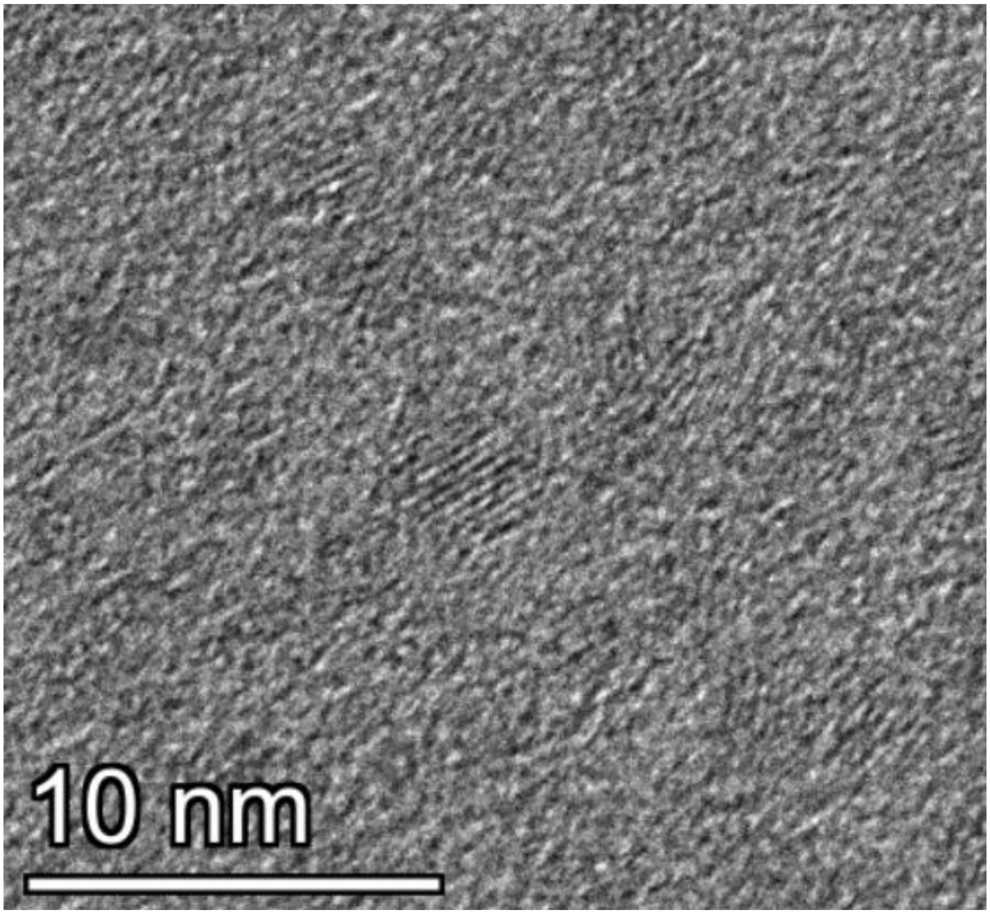

Figure 16. HRTEM photograph of 325℃ CeO_{2-X}.

Due to the large broadening of the XRD peaks, HRTEM was used to collect further structural data to determine the crystal structure, morphology, and particle size of the NCs. However, it was found that the HRTEM showed poor contrast making it difficult to gather any useful data. Otherwise, the average particle size was approximately 3 nm and the morphology was quasi-spherical. The morphology was not unexpected, since for smaller particle sizes of CeO_2 the quasi-spherical morphology is preferred[47,52].

3.2 Optical and Magneto-optical Properties of CeO_{2-X} Nanocrystals

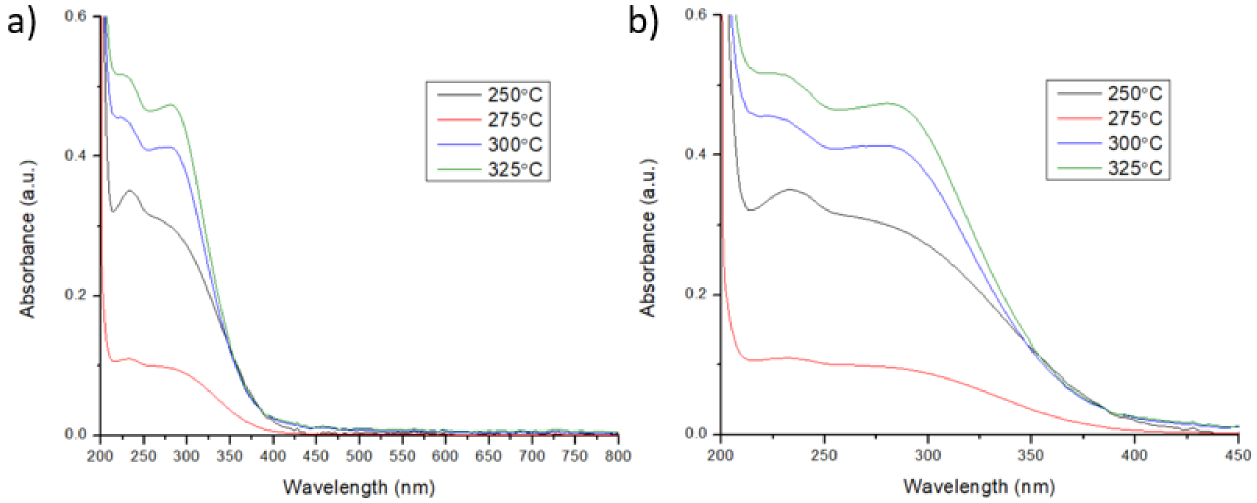

Figure 17. UV-vis absorbance of colloidal CeO_{2-X} NCs synthesized at various reaction temperatures ranging from a) 200 - 800 nm and b) 200 - 450 nm.

Absorbance data was obtained for all four temperatures and for each sample there was a gradual decrease in absorption from 350 nm and throughout the visible range. CeO_{2-x} is known for its redox reversibility between Ce^{4+} and Ce^{3+} ions in the ground state, and oxygen vacancies will naturally form due to imperfection in the crystal lattice. When an oxygen vacancy forms, a nearby Ce^{4+} ion will have an extra unreacted bond which will then reduce Ce^{4+} to Ce^{3+}. [53] It could be said the Ce^{3+} ions and the neighbouring oxygen vacancies act as coupled point defects.[45] The main features in the spectrum are two absorption peaks at 281 nm and 231 nm. Depending on the sample, the peak position may shift by a few nm and the shape of the absorption features will either be a shoulder or a peak. The lower and higher temperature samples showed an inverse relationship with the shape of their peaks. For samples below 275℃, the 282 nm peak appears as a shoulder, and the 231 nm peak is more pronounced. While for samples above 300˚C the opposite is observed, the 282 nm peak is more pronounced, and the 231 nm peak becomes a shoulder. The change in shape might be due to changing the amount of sub states below each transition and broadening the peaks. The increase in absorption at 281 nm is caused by the increasing the concentration of Ce^{3+} defects and hence increasing the population of electrons occupying the Ce 4f mid-band gap states. Since the 281 nm peak increases with increasing reaction temperature, along with the particle size, it appears having a larger crystal size is associated with having a higher population of Ce 4f electrons.

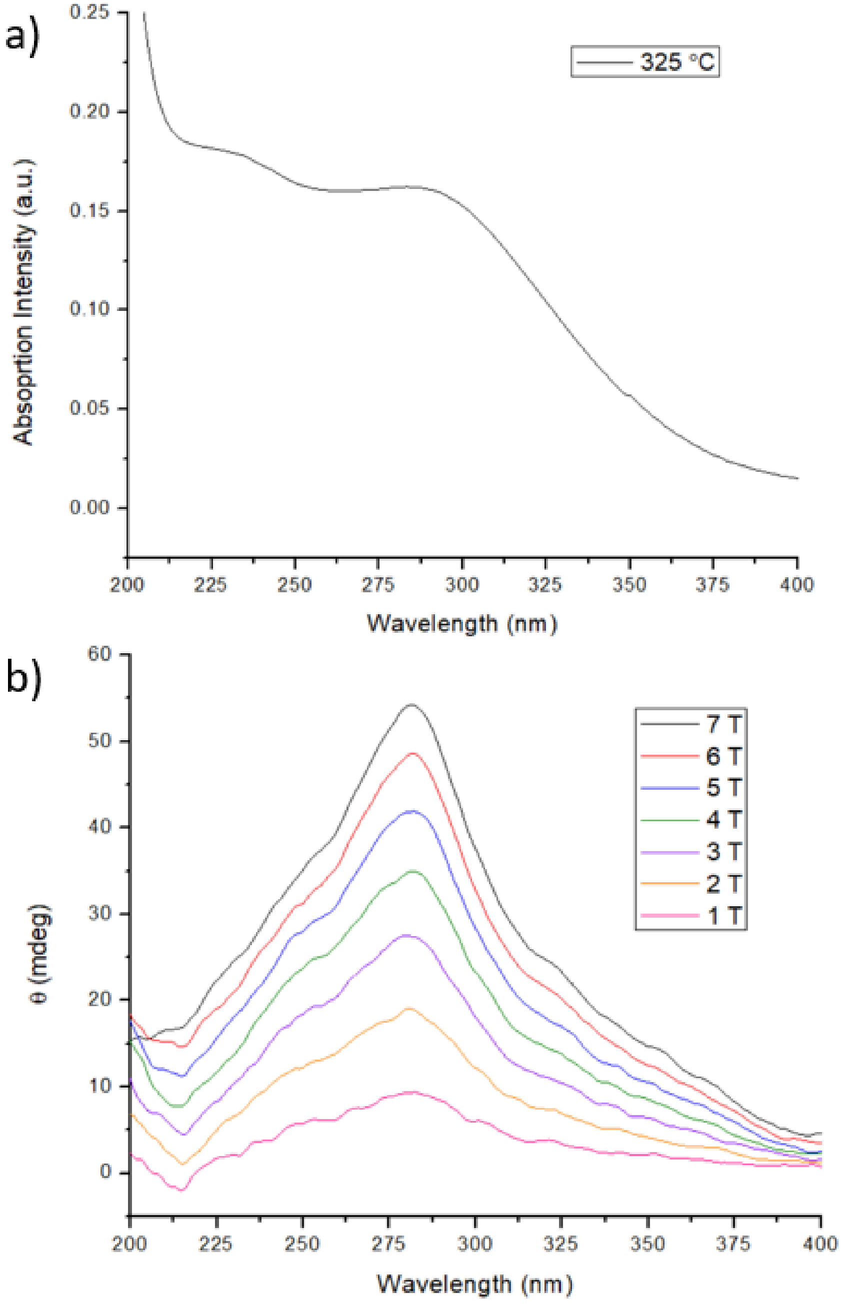

Figure 18. UV-vis absorption and b) variable-field MCD spectra of colloidal 325℃ CeO_{2-x} measured at 5 K from 1 to 7 T.

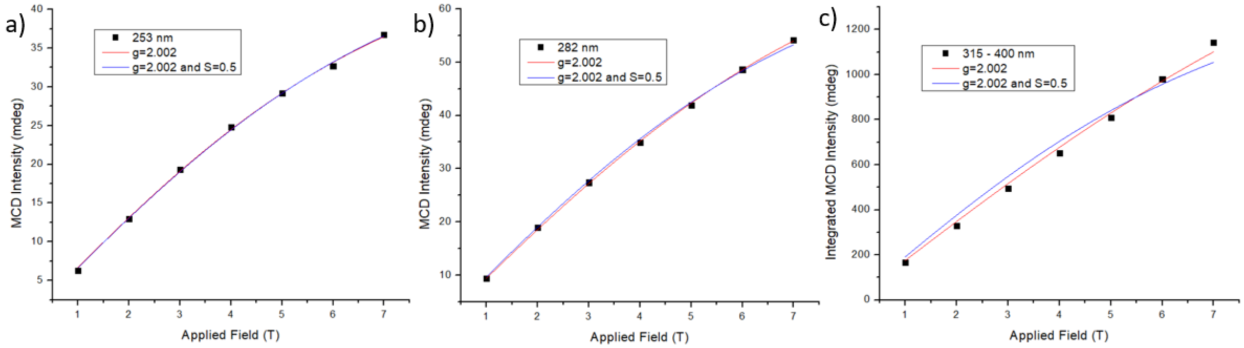

Figure 19. Field dependent MCD peak intensity plotted at a) 253 nm, b) 282 nm, and integrated MCD peak intensity from c) 315-400 nm.

Observed from the field dependent MCD data in Figure 18, one large convoluted MCD peak at 282 nm with only positive parity was present, along with two broad regions with shoulder peaks (315–400 nm and 215–260 nm). By plotting the MCD peak intensity at 253 and 282 nm, the two peaks had fitted for g=2.002 ad S=0.5, showing both peaks are paramagnetic in nature. To note, the 253 nm peak was plotted monochromatically since it showed the most saturation at that wavelength. Despite not having same peak intensity, the 253 and 282 nm peaks had the same magnetic saturation. The two peaks are likely C-terms due to their paramagnetic nature, as paramagnetic samples often show C-term MCD peaks. Although to confirm if the peaks are C-terms, temperature dependent MCD will need to be collected. The 282 and 253 nm peaks might correspond to Ce^{3+} species due to Ce^{3+} having only one unpaired 4f electron, while Ce^{4+} has no unpaired electrons and is diamagnetic. As a first estimate, the 282 nm peak is likely the excitation of a single electron from the O 2p valence band to the unoccupied Ce 4f states. While the 252 nm peak is transition from the occupied Ce 4f states to the Ce 5d conduction band. The broadness of the 215-260 nm peak is possibly from different localized states in-between the Ce 4f and Ce 5d states.

However, when trying to fit the 315–400 nm shoulder region, even with using integrated MCD intensity to include more signal, the data was unable to fit for g=2.002 and S=0.5. The data fitted linearly, which means the peak is delocalized in nature and somehow the charge carriers are polarized.[50] Temperature dependent MCD would be required to help determine if the region is possibly an A- or B-term as A- and B-terms are temperature independent. Although, considering the energy position of the regions suggest the gradual absorption of sub-band gap states below the O 2p valence band. It was reported that ZnO films also showed a low intensity MCD peak below the valence band and hypothesized it came from singly occupied oxygen vacancy defects.[28]

In summary, structural, optical, and magneto-optical characterization was performed on colloidal CeO_{2-X} NCs. It was found that by changing the synthesis temperature, the peak intensity and shape of the 281 and 231 nm absorption peaks from UV-vis had an inverse relation. Additionally, it was found larger/higher temperature NCs have a larger population of Ce^{3+} due to the increased absorption of the 281 nm peak. From the field dependent MCD data, one large MCD peak was centered at 282 nm that was neighboured by two broad regions from 215-260 nm and 315-400 nm. The 282 nm peak matched the energy position of the 281 nm UV-vis absorption peak and is likely the O 2p to Ce 4f (unoccupied transition). While the 215-260 nm region suggests there are multiple peaks between the Ce 4f mid-band states and the Ce 5d conduction band. Finally, the 315-400 nm region was the most elusive, as the fitted MCD peak intensity deviated from a Brillouin fitting of $g=2.002$ and $S=0.5$ and was delocalized in nature. To further explore the nature of these transitions and their MCD-terms, obtaining temperature dependent MCD is required. Despite this, comparing the MCD spectra of colloidal CeO_{2-X} with small crystal domain size to the following annealed CeO_{2-X} powders will help further elucidate how grain size affects the room-temperature ferromagnetic-like ordering.

Chapter 4

Annealed Magnetic CeO_{2-X}

4.1 Annealing Time Series

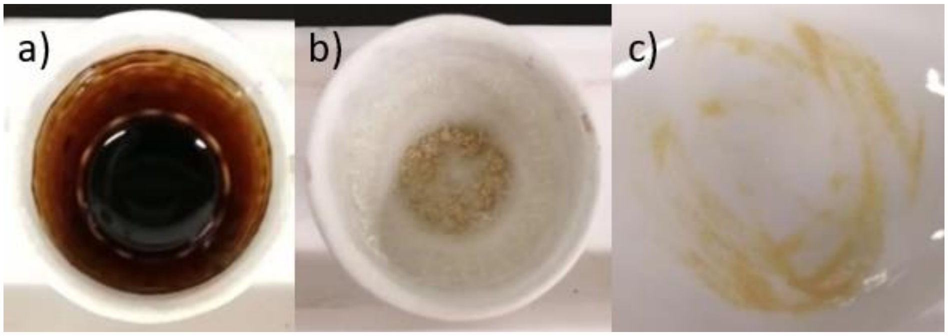

Figure 20. Appearance of a) non-annealed CeO_{2-X} NCs, b) annealed CeO_{2-X} for 24 hours at 800℃, and c) ground CeO_{2-X} powder.

In this section, colloidal CeO_{2-X} NCs synthesized at 325°C, chosen for having the best crystallinity, were annealed in three different annealing series: time, temperature, and atmosphere. This was done to systematically control each parameter and observe how the magnetic response changed with crystal size and defect concentration. For the first series, 800°C was the control temperature used in the time series since it was reported that CeO_2 achieves the highest crystallinity at this temperature.[54] On top of this, the time series was conducted by annealing a single sample cumulatively up to 48 hr to control for the initial concentration of defects.

In the first step of the time series, after annealing CeO_{2-X} NCs for 1 hour at 800℃ in ambient air, the sample became a pale yellow crystalline powder. The magnetic properties were measured using PPMS, and then reannealed for longer times consecutively up to 48 hours (1 hr, 8 hr, 24 hr, and 48 hr). As the sample was annealed longer, the colour slowly became whiter. This is likely due to more oxygen vacancies being filled in over time. Which means the red amber/ yellow amber colour prior to annealing is indeed caused by the amount of oxygen vacancies. For samples with a high concentration of oxygen vacancies, the colour is a pale yellow and samples with a low concentration of oxygen vacancies are white.

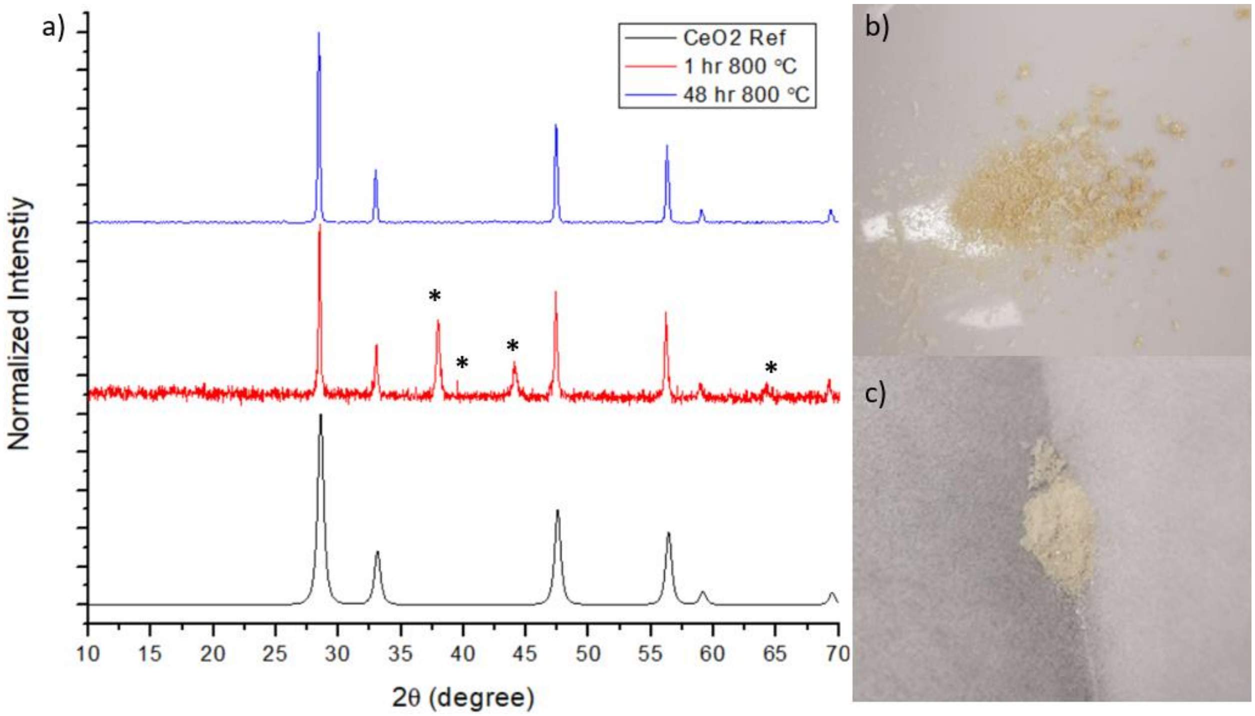

Figure 21. XRD of annealed CeO_{2-X} for 1 hr and 48 hr at 800℃ in ambient air. Peaks from the aluminum substrate are labelled with an asterisk (*).

XRD was obtained for 1 hr and 48 hr annealed samples, and immediately it was noted that the annealed samples had significantly higher and narrower peaks compared to non-annealed CeO_{2-X} NCs. The peaks matched the cubic phase of CeO_2 and all peaks were present. The peaks in the 1 hr XRD pattern at 38.59°, 44.86°, and 65.32° were from the aluminum substrate. After 1 hr annealing, the NCs had become a bulk powder.

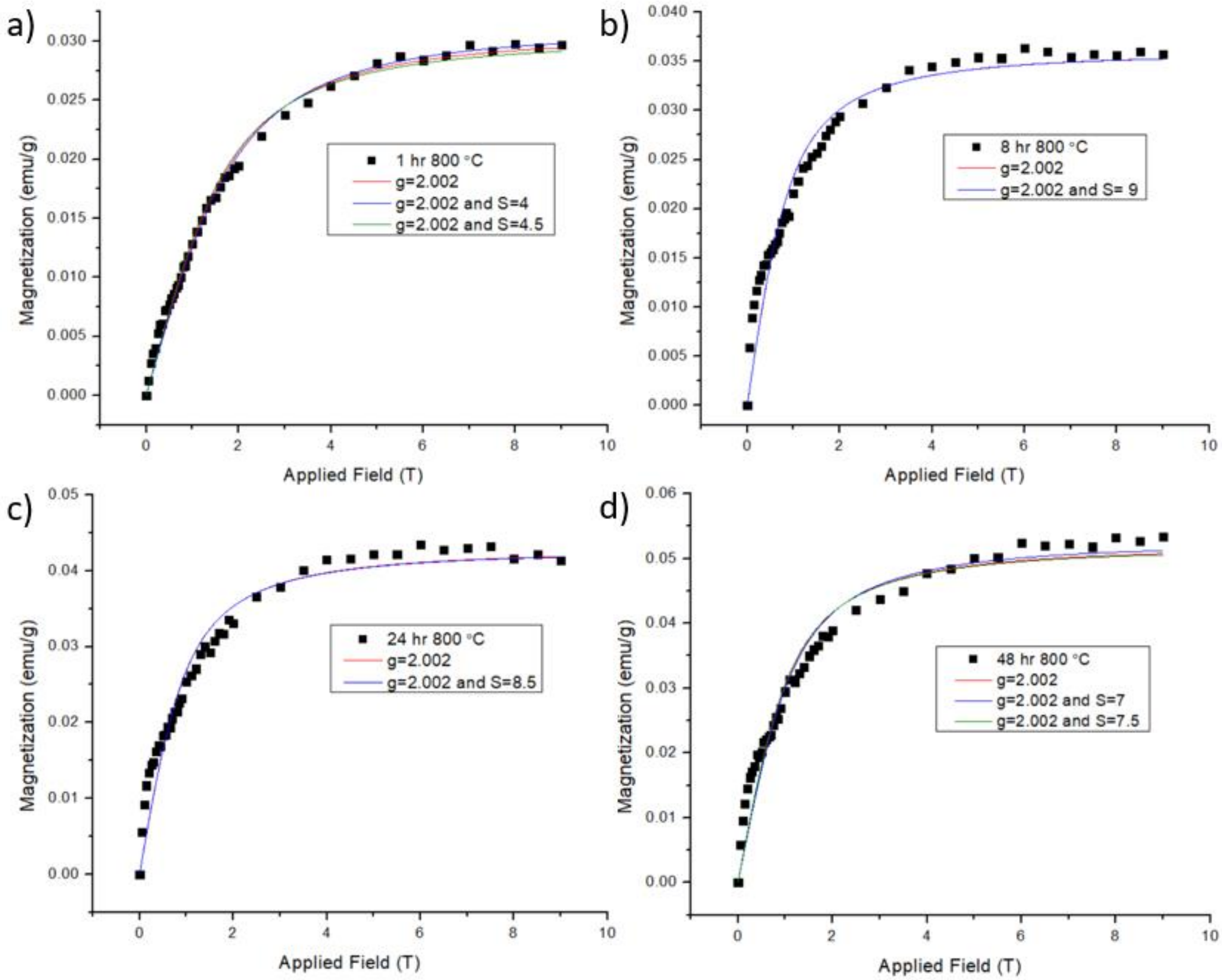

Figure 22. Magnetization saturation measured at 2 K of CeO_{2-X} annealed at 800°C for a) 1 hr, b) 8 hr, c) 24 hr, and d) 48 hr.

Magnetic saturation curves from 0 to 9 T were obtained after each annealing cumulatively up to 48 hr by subtracting out any diamagnetic or paramagnetic component from the raw M-H curves. Unexpectedly an interesting behaviour was observed in each saturation curve, where there was a degrading fit quality of the Brillouin function, and an increasing a kink in the curve between 0-0.75 T, shown in Figure 22. The segment was removed and the curves refitted to see if the spin (S), magnetic saturation (M_S), and population of centers (N) changed. Shown in Figure 23, the "superparamagnetic" component of each annealing showed the same trend even though the spin values decreased slightly.

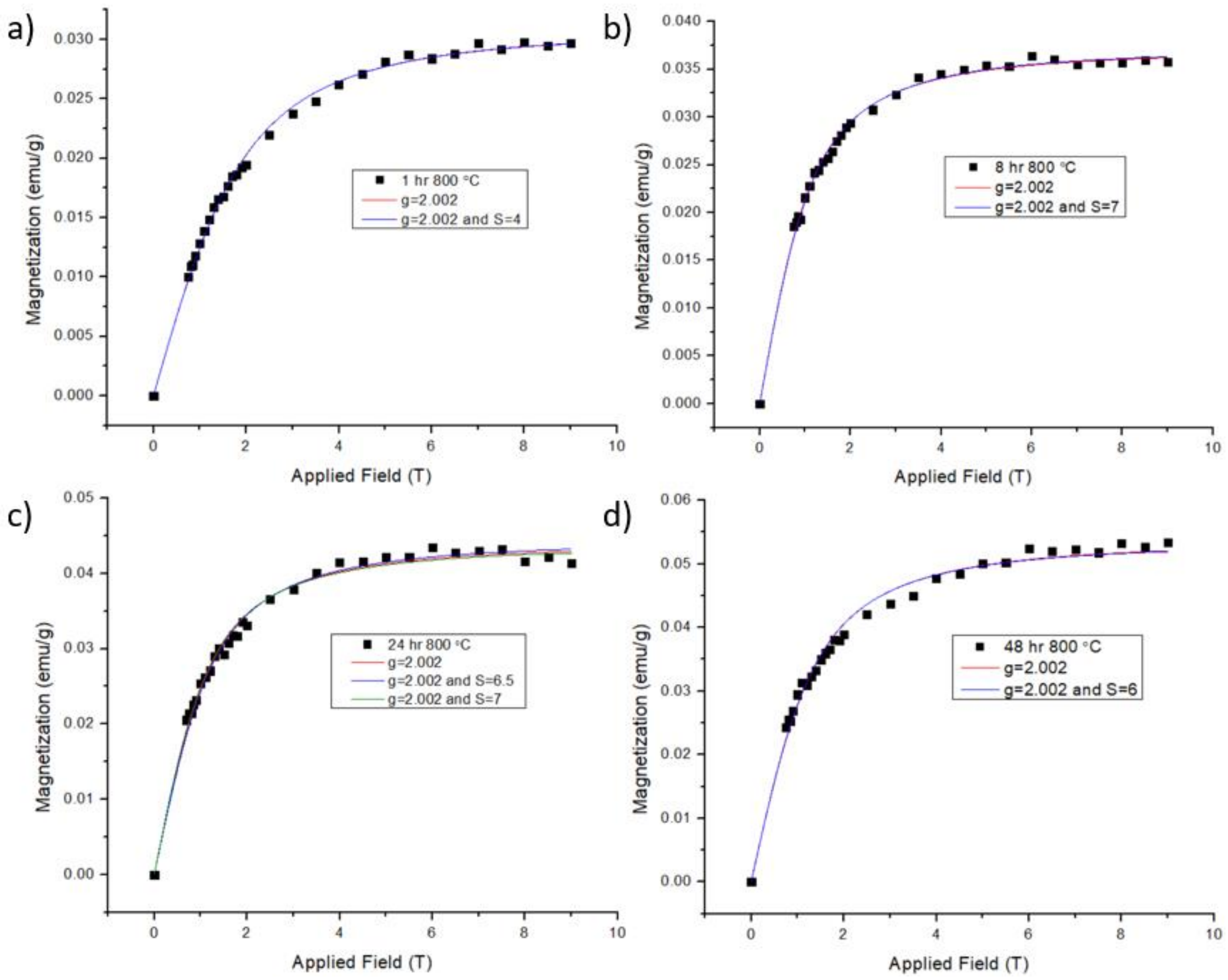

Figure 23. Magnetization saturation data of the isolated superparamagnetic component measured at 2 K of CeO_{2-X} annealed at 800°C for a) 1 hr, b) 8 hr, c) 24 hr, and d) 48 hr.

The removed kink seemed to appear systematically, so the segment was isolated and refitted separately from the superparamagnetic component as shown below in Figure 24, and labelled as the "ferromagnetic-like" component. In some cases, the range of the ferromagnetic-like component deviated by 1 or 2 data points between samples, but otherwise the trend of the spin values gradually increased with annealing time. Compared to the superparamagnetic component, the spin values dramatically increased, for example from the 8 hr annealing time, S = 61 (ferromagnetic-like) vs. S = 7 (superparamagnetic).

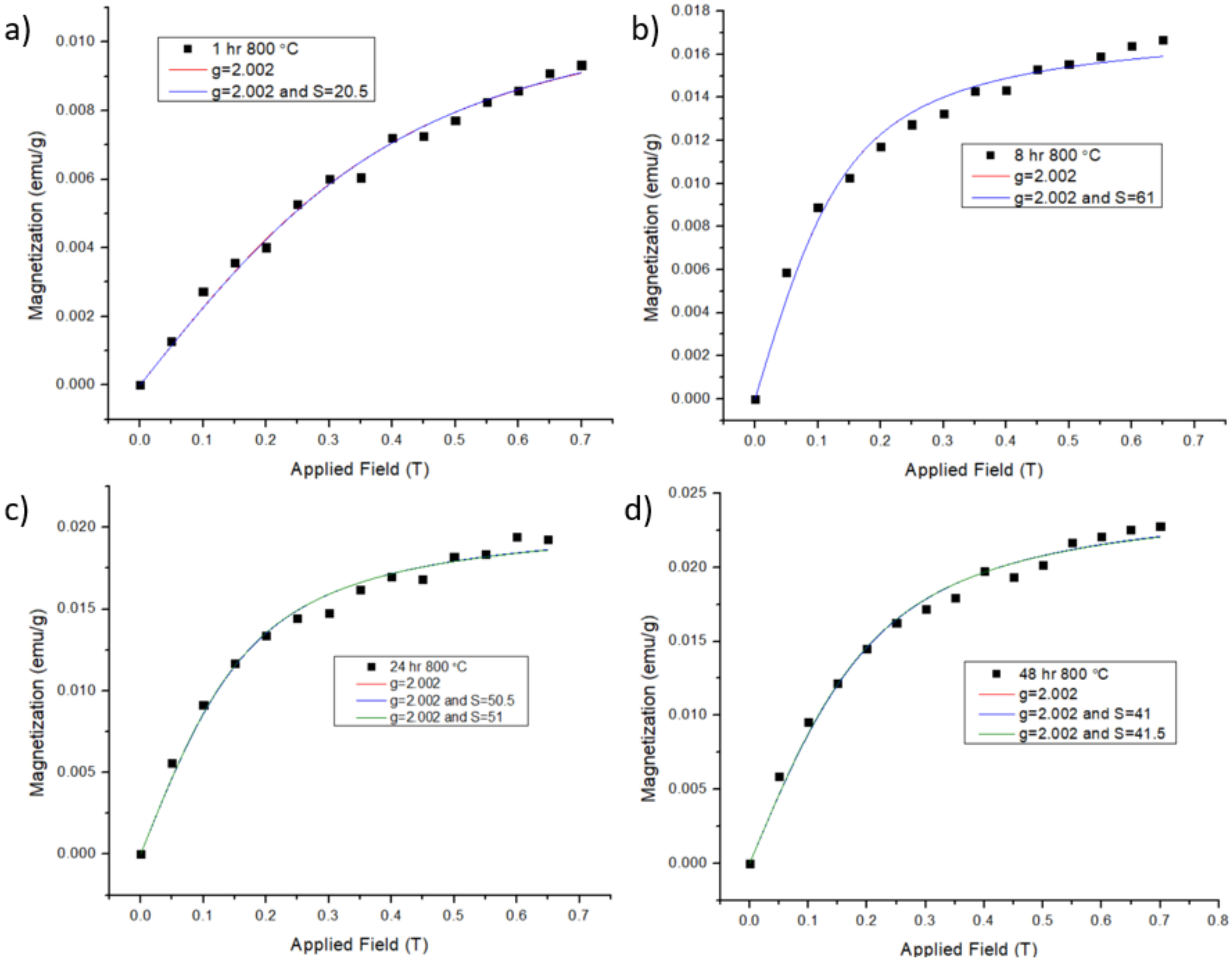

Figure 24. Magnetization saturation data of the isolated ferromagnetic-like component measured at 2 K of CeO_{2-X} annealed at 800˚C for a) 1 hr, b) 8 hr, c) 24 hr, and d) 48 hr.

Sample	Superparamagnetic S	Ferromagnetic-like S
1 hr	4	20.5
8 hr	7	61
24 hr	6.5/7	50.5/51
48 hr	6	41/41.5

Table 1. Comparison of spin values between the superparamagnetic and ferromagnetic-like components of the time annealed series.

Sample	Superparamagnetic N	Ferromagnetic-like N	% Supermagnetic Contribution	% Ferromagnetic-like Contribution
1 hr	2.0E20	1.6E19	92.0	8.0
8 hr	1.4E20	7.7E18	94.5	5.5
24 hr	1.7E20	1.1E19	93.5	6.5
48 hr	2.4E20	1.6E19	93.3	6.7

Table 2. Comparison of N values between the superparamagnetic and ferromagnetic-like components of the time annealed series.

Sample	Superparamagnetic M_S (emu/g)	Ferromagnetic-like M_S (emu/g)	% Superparamagnetic Contribution	% Ferromagnetic-like Contribution
1 hr	0.02967	0.00933	68.55	31.45
8 hr	0.03575	0.01666	53.40	46.60
24 hr	0.04327	0.01929	55.42	44.58
48 hr	0.05346	0.02278	57.39	42.61

Table 3. Comparison of M_S values between the superparamagnetic and ferromagnetic-like components of the time annealed series.

After fitting both components, all parameters (S, M_S, and N) were collected into the above tables and then compared in different plots of how S, M_S, and N changed between the superparamagnetic and ferromagnetic-like component. The contribution percentage of S, N, and M_S was calculated by dividing, for example the N of ferromagnetic-like centers by the N of superparamagnetic centers, and multiplied by 100. Then the contribution of the superparamagnetic component was calculated by subtracting 100 by the ferromagnetic-like percentage contribution.

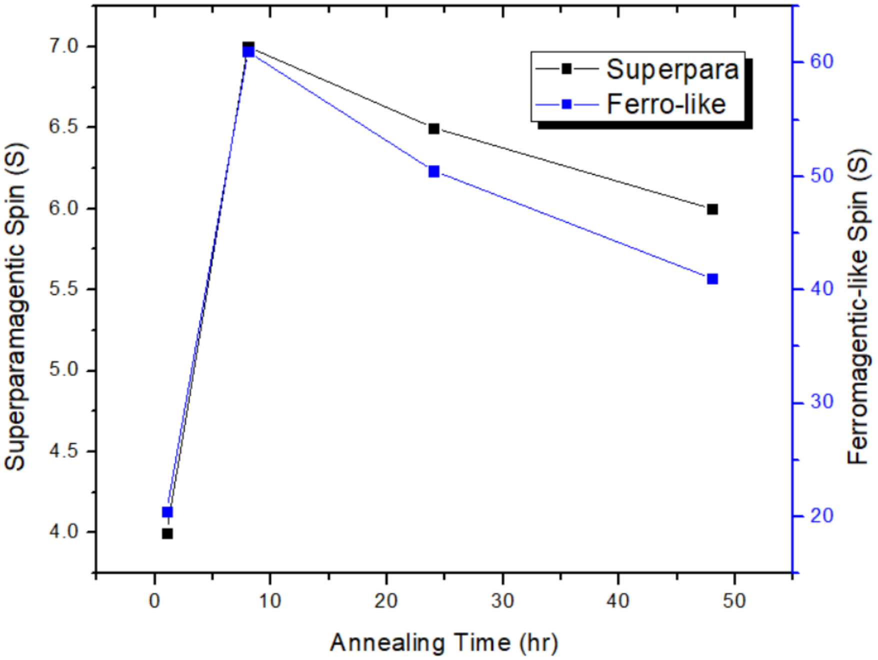

Figure 25. Spin values (S) of time annealing series.

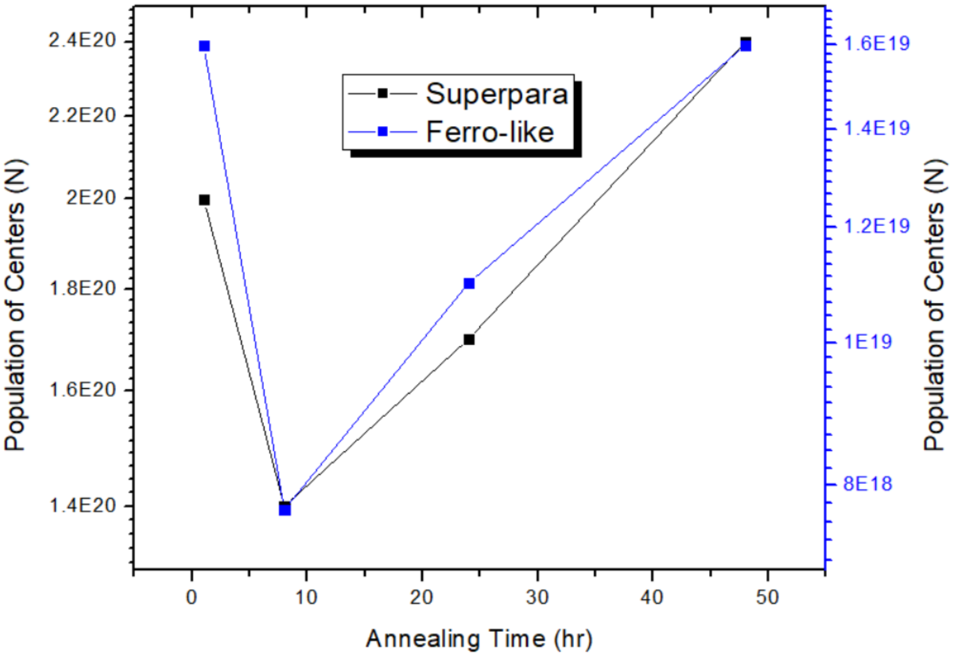

Figure 26. Population of centers (N) of time annealing series.

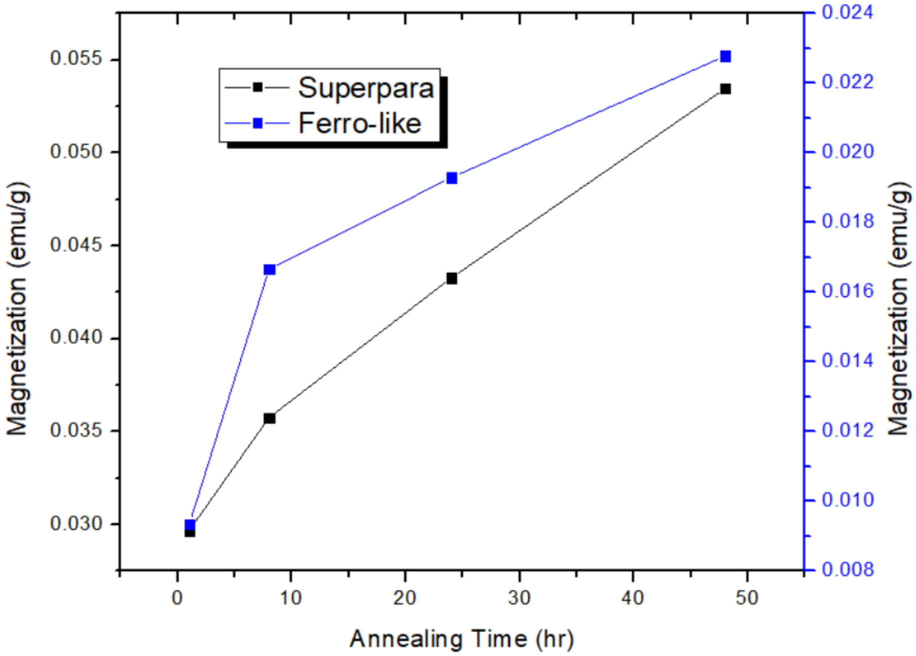

Figure 27. Magnetization (M_S) of time annealing series.

The largest increase in spin occurred between 1 hr and 8 hr annealing time, and slowly decreased afterwards for both the superparamagnetic and ferromagnetic-like component. From 1 hr to 8 hr, the increase in spin was caused by defects migrating into clusters. Then after 8 hr annealing, the defects finished migrating, and the spin of the magnetic centers began to decrease due to excess annealing slowly filling in oxygen vacancies and lowering the number of defects that could contribute to the total spin. Then comparing the population of centers (N), initially the value of N decreased for both components, but after 8 hr annealing the value of N increased again. The value of N should not be taken too seriously considering N in the spin only Brillouin function is mainly used as a free-floating scaling factor. So as the total magnetization increases, the value of N would also increase which can be seen in the magnetization trend. Lastly, it was observed that the magnetization of both components increased with further annealing. There is a sharper increase from 1 hr to 8 hr annealing in Figure 27. similar to the trend for the spin values, but in this case the magnetization gradually increases with longer annealing.

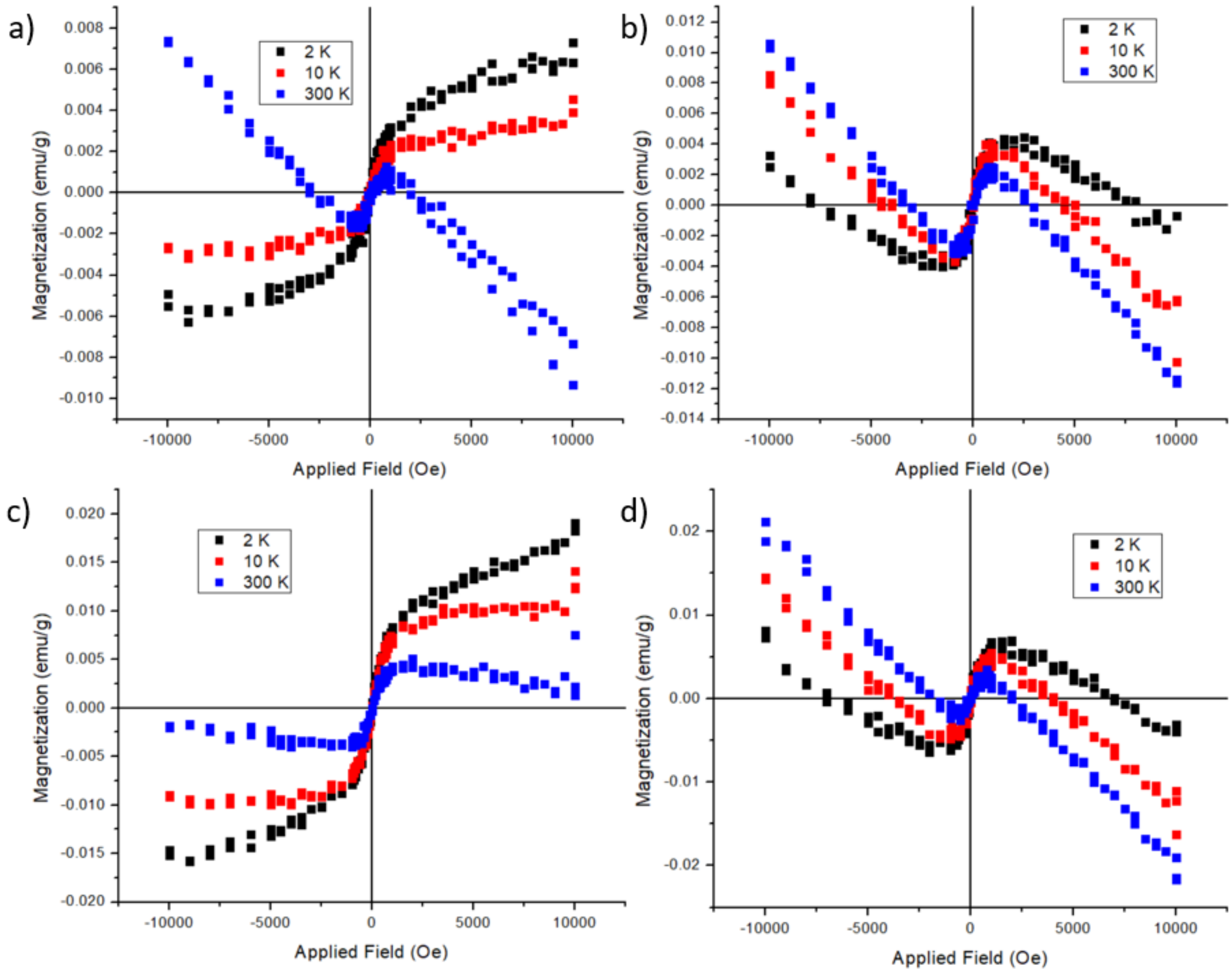

Figure 28. Raw data of -1 to +1 T magnetic sweep measurements of annealed CeO_{2-X} at 800˚C for a) 1 hr, b) 8 hr, c) 24 hr, and d) 48 hr.

Following the 0-9 T magnetic saturation measurements, magnetic sweep measurements were collected between -1 to 1 T at 2, 10, and 300 K. The raw data was later corrected by subtracting out any diamagnetic or paramagnetic contribution. But before any corrections, the 24 hr annealing showed the highest magnetic saturation.

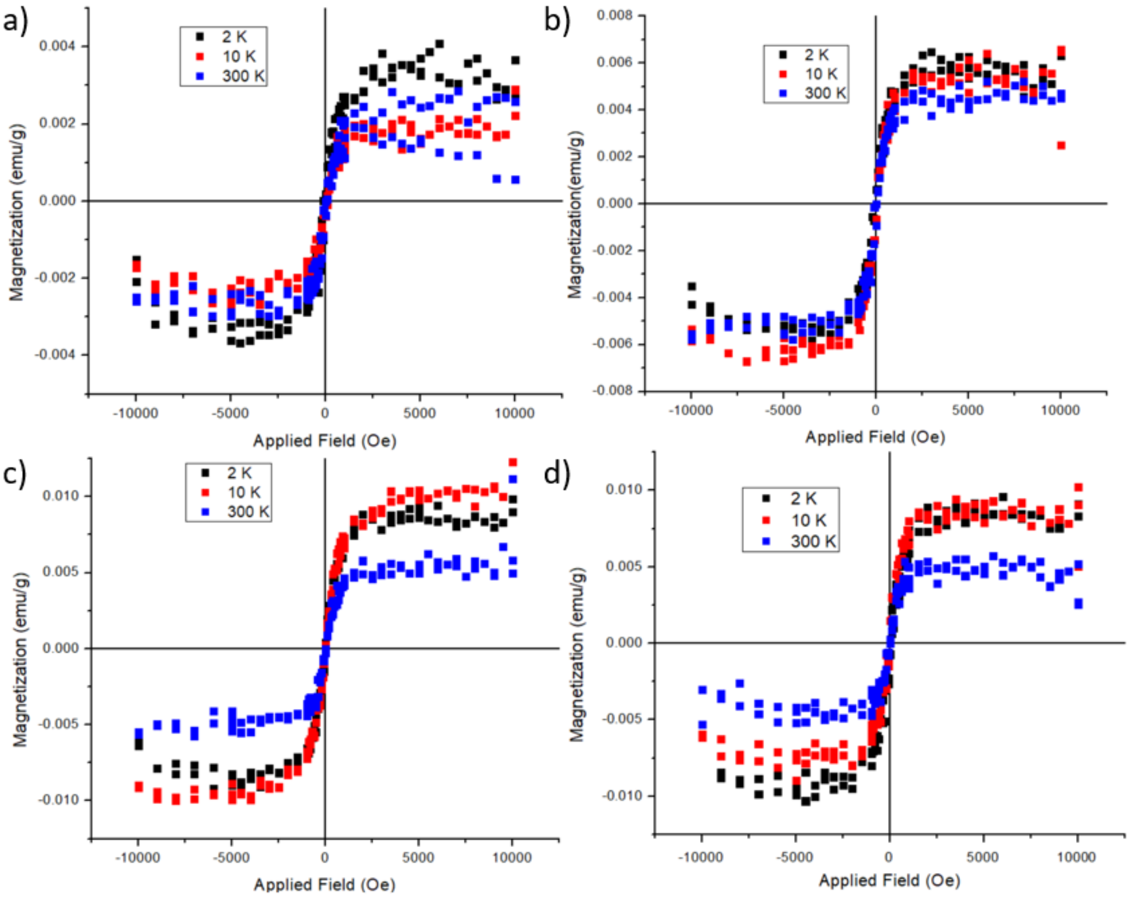

Figure 29. Corrected data of -1 to +1 T magnetic sweep measurements of annealed CeO$_{2-X}$ at 800 ˚C for a) 1 hr, b) 8 hr, c) 24 hr, and d) 48 hr.

After correcting the data, all annealing times showed ferromagnetic-like behaviour at room temperature (300 K), and a higher magnetic signal at lower temperatures, 2 K and 10 K. With decreasing temperature, the magnetic saturation will increase for Curie type behaviour. At 300 K only centers that are contributing to the ferromagnetic-like signal are coupling. But as the temperature decreases, the superparamagnetic component, which is temperature dependent and behaves like paramagnetism, will increase in intensity as the temperature decreases. For all samples at 300 K the magnetic saturation was consistently around 0.005 emu/g, so this additional evidence of multiple components contributing to the total magnetization.

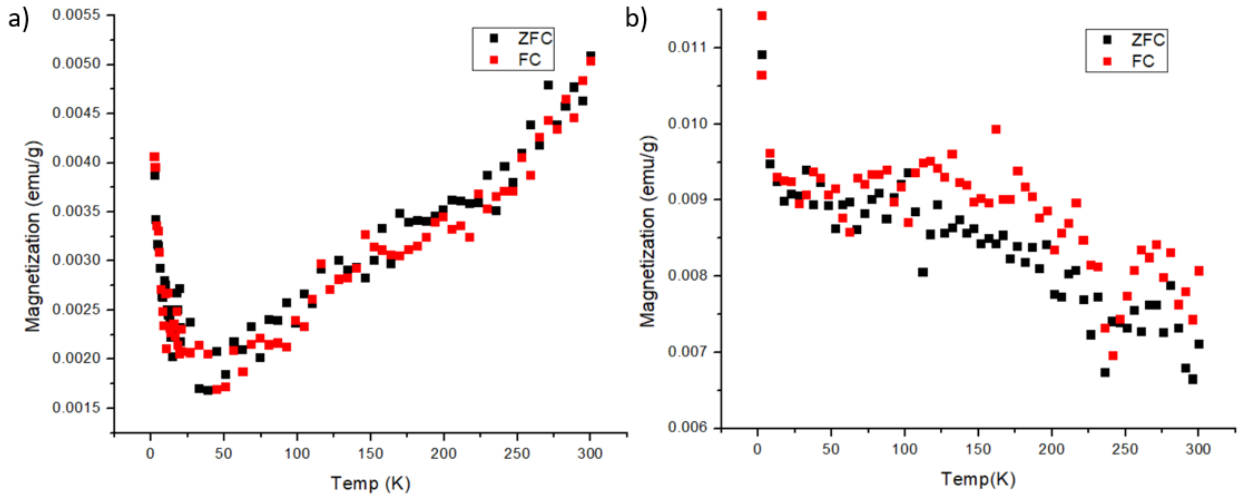

Figure 30. ZFC and FC measurements of annealed CeO_{2-X} at 800°C for a) 1 hr and b) 24 hr under 1500 Oe.

To investigate the Curie temperature, zero-field cooling and field cooling (ZFC/FC) measurements were conducted for 1 hr and 24 hr annealed CeO_{2-X}. Neither sample showed separation between ZFC and FC, which is a typical behaviour of ferromagnetic materials. In Figure 30.b), 24 hr showed slight separation between the two curves however the data is very noisy so it is hard to make any conclusions. While for the 1 hr sample, the signal had less noise and showed an interesting trend. It appeared the magnetization decreased from 300 K to approximately 45 K, and then suddenly increases again. The transition at 45 K might be due to a low temperature phase transition in the crystal structure and thus changing the superexchange interactions from antiferromagnetic to ferromagnetic. Temperature dependent XRD has been reported for nanosized CeO_2 of a reversible tetragonal to cubic phase transition that occurs between 200 K to 250 K.[55] But for bulk crystals, this change was not observed and the authors only measured down to 75 K.[55] So further investigation with additional temperature dependent XRD would be needed to determine if there is another phase transition at temperatures lower than 75 K. Another observation was how the behaviour changed completely between the 1 hr and 24 hr annealing. For the 24 hr annealed sample, the magnetic signal slowly increased from 300 K to 25 K, and rapidly increased below 25 K. The gradual increase in magnetization matched the same trend found in the -1 to 1 T magnetic sweep measurements, and suggests there is a possible Curie temperature above 300 K.

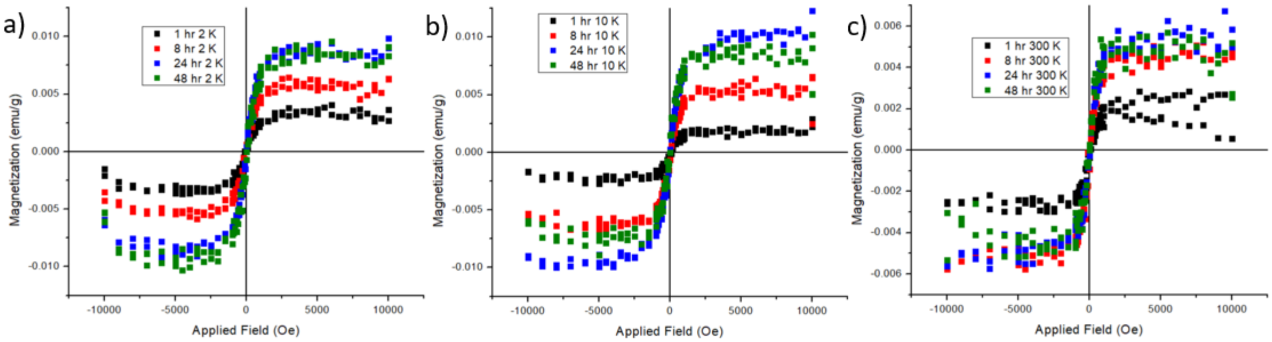

Figure 31. Comparison of magnetic sweep data of CeO_{2-X} time annealed measured at a) 2 K and b) 10 K, and c) 300 K. Black is 1 hr, red is 8 hr, blue is 24 hr, and green is 48 hr.

From comparing each annealing, the magnetic response increased with longer annealing time up to 24 hr. It appears having larger grain sizes or providing more time to allow defects to migrate enhanced the ferromagnetic-like ordering. After 24 hr, the signal at 2 K, 10 K, and 300 K, stopped increasing and saturated up to 48 hr. Overall, 24 hr annealing time across all temperatures: 2 K, 10 K, and 300 K, showed the highest magnetic response. In some cases, 8 hr or 48 hr were comparable in intensity but comparing the raw data of the magnetic sweep measurements, the 24 hr sample had significant ferromagnetic-like response (0.006-0.01 emu/g) across all temperatures without any corrections. On top of which, 24 hr annealing had high spin values for both the ferromagnetic-like and superparamagnetic components (S=50.5/51 and S=6.5/7, respectively). Thus, 24 hr annealing time was chosen as the control for the next experiments conducted in the CeO_{2-X} temperature annealing series.

4.2 Annealing Temperature Series

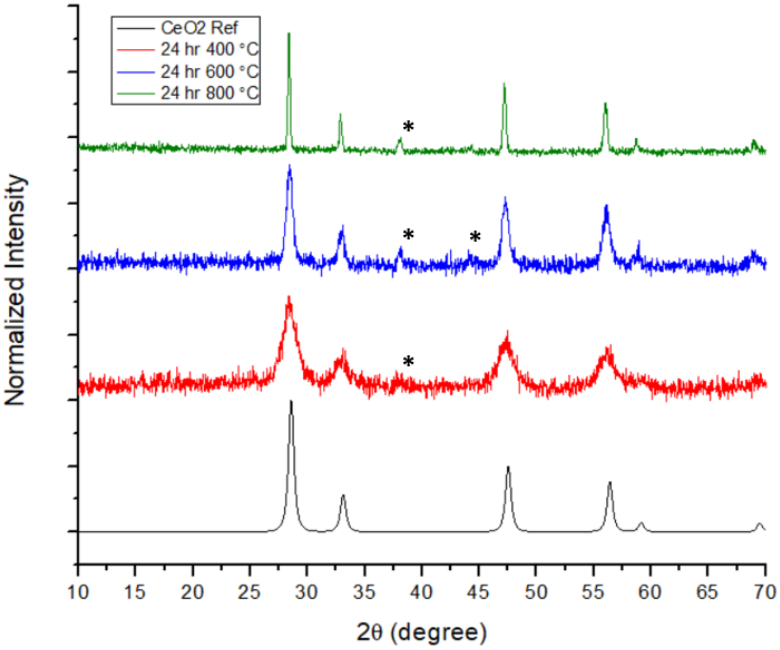

Figure 32. XRD of CeO_{2-X} temperature annealed series. Peaks from the aluminum substrate were labelled with an asterisk (*).

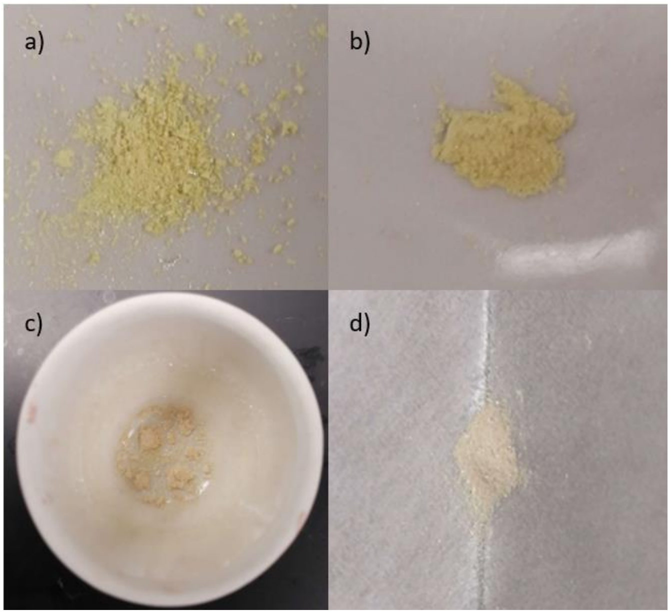

Figure 33. Physical appearance of CeO_{2-X} annealed at a) 400℃, b) 600℃, c) 800℃, and d) 1000℃ for 24 hr in air.

The temperature annealing series was conducted by annealing several samples for 24 hr in air at different temperatures: 400˚C, 600˚C, 800˚C, and 1000˚C. All samples were sister samples prepared from the same colloidal batch to control for initial defect concentration. XRD was first collected and compared in Figure 32., there was a clear crystal size difference dependent on the annealing temperature. At first, 400˚C annealing showed broad peaks similar to unannealed CeO_{2-X} NCs. However immediately, 600˚C showed narrower peaks and was closer to bulk cubic CeO_2. It appeared using 400˚C the heat is only enough to boil off the surface ligands and not enough to sinter the NCs together. This was not unexpected since Olam and Olac boil at 364˚C and 360˚C, respectively.[47] While using 600˚C provided enough heat to form Ce-O bonds and make larger grains. By using higher annealing temperatures, 800˚C and 1000˚C provided plenty of energy to efficiently form Ce-O bonds to get the highest crystallinity, which was also observed in literature.[51]

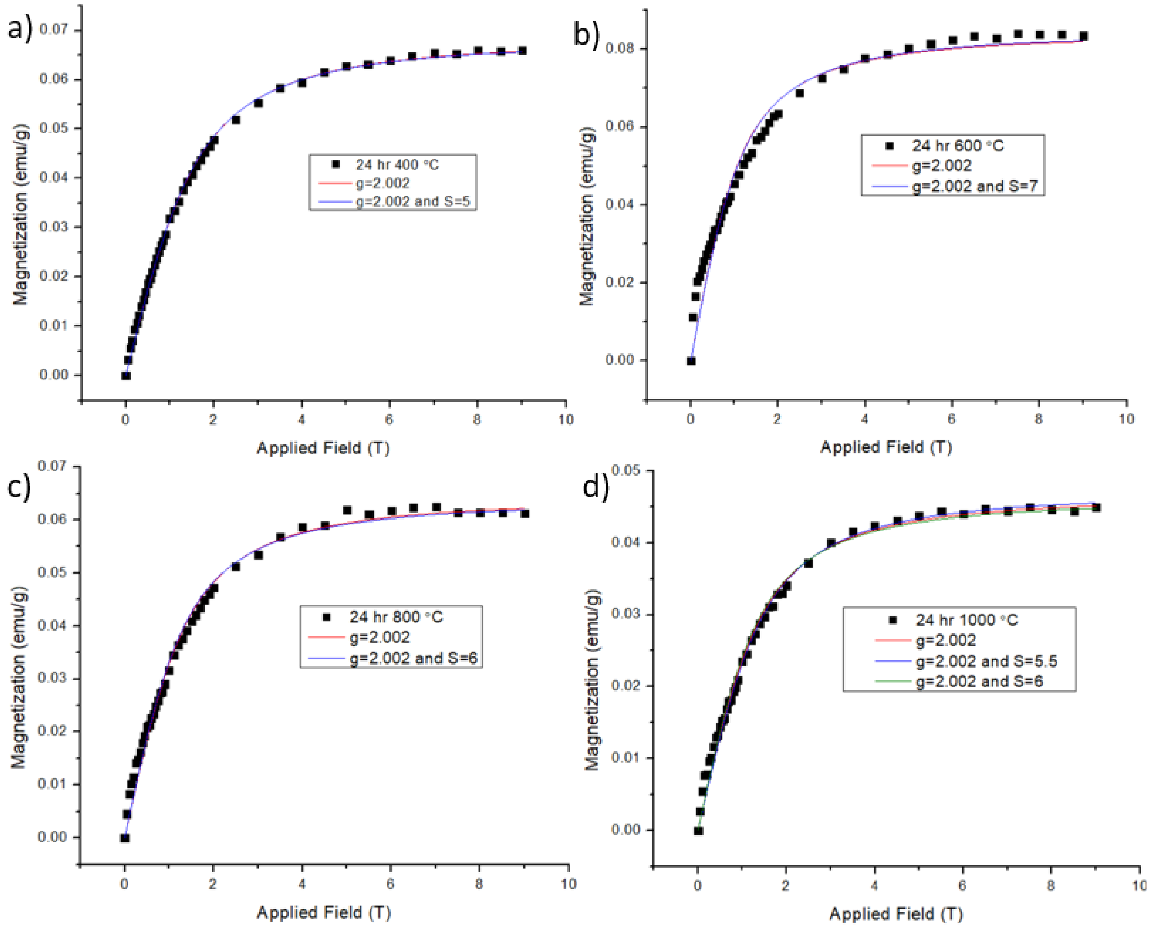

Figure 34. Magnetic saturation measured from 0-9 T at 2 K of CeO_{2-X} annealed at a) 400℃, b) 600℃, c) 800℃, and d) 1000℃ for 24 hr.

Just like the time annealing series, the temperature series showed a kink between 0 – 0.7 T for samples annealed above 600˚C. So, the kink region was removed and the ferromagnetic-like and superparamagnetic regions were isolated and refitted using the Brillouin function.

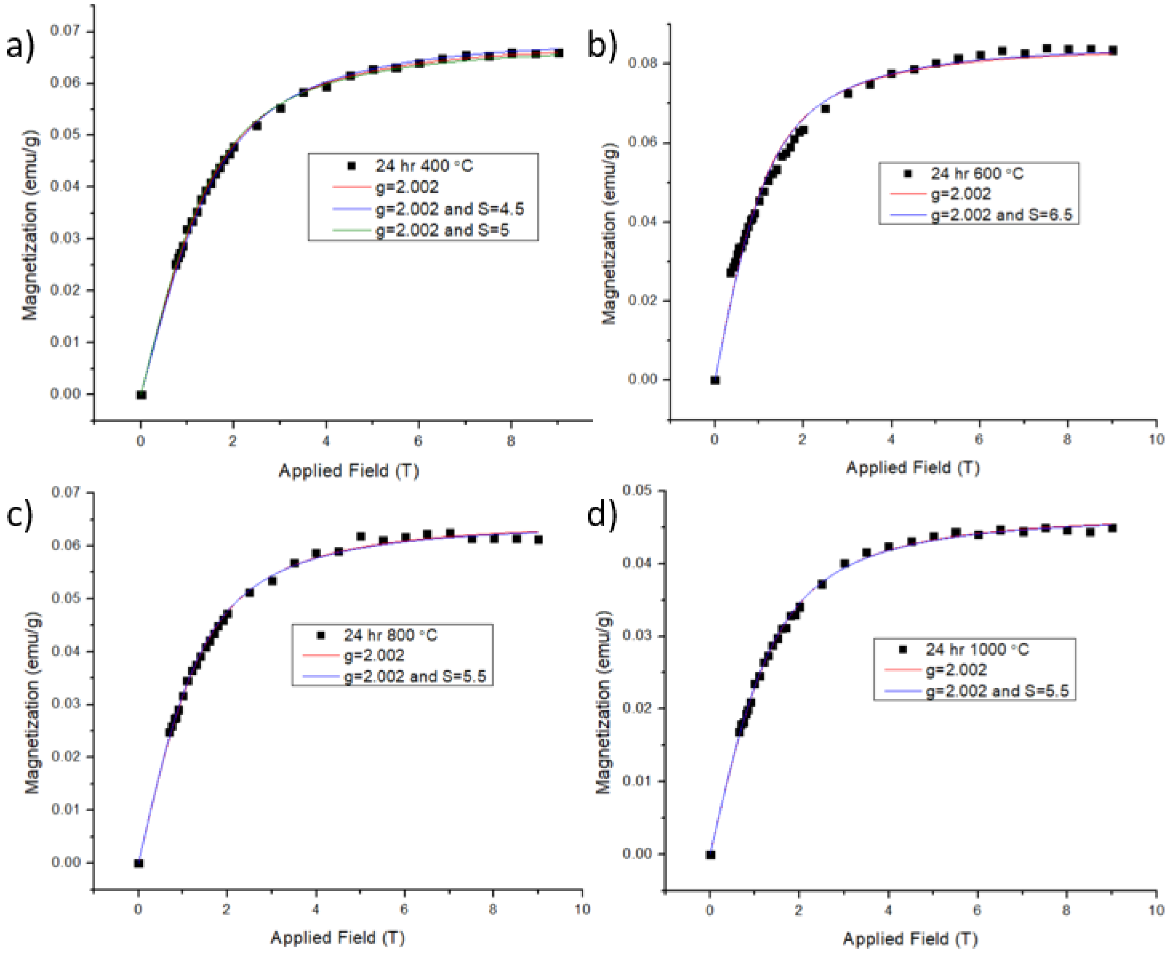

Figure 35. Magnetic saturation of the isolated superparamagnetic component of CeO$_{2-X}$ annealed at a) 400℃, b) 600℃, c) 800℃, and d) 1000℃ for 24 hr in air.

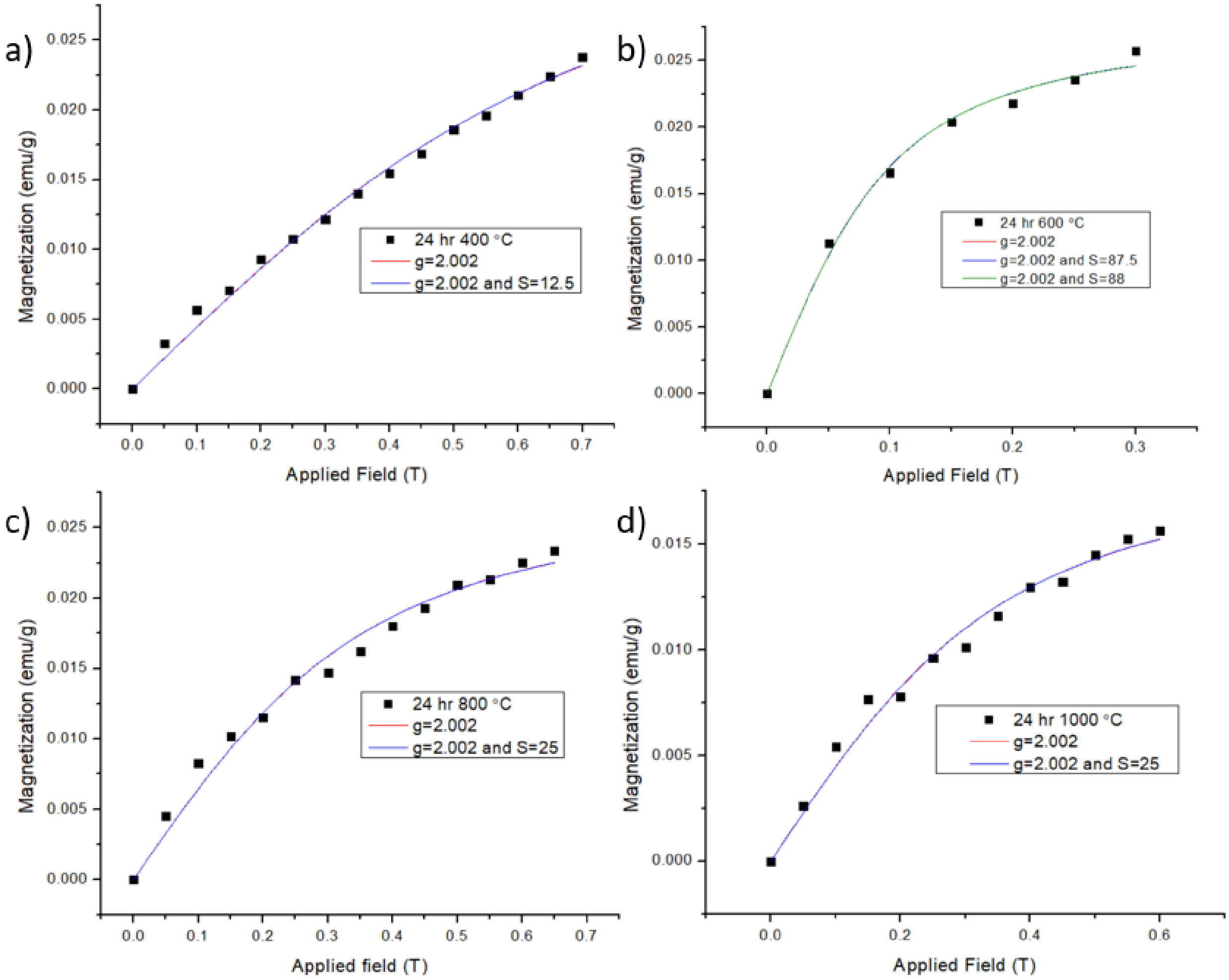

Figure 36. Magnetic saturation of the isolated ferromagnetic-like component of CeO_{2-X} annealed at a) 400℃, b) 600℃, c) 800℃, and d) 1000℃ for 24 hr.

Again, there was a huge difference in spin values between the superparamagnetic and ferromagnetic-like regions. To note, when fitting the ferromagnetic-like component of the 600 C sample extra data points were removed to get a proper fit of the saturation.

Sample	Superparamagnetic S	Ferromagnetic-like S
400℃	4.5/5	12.5
600℃	6	87
800℃	5.5	25
1000℃	5.5	25

Table 4. Comparison of spin values between the superparamagnetic and ferromagnetic-like components of the temperature annealed series.

Sample	Supermagnetic N	Ferromagnetic-like N	% Superparamagnetic Contribution	% Ferromagnetic-like Contribution
400℃	3.6E20	7.9E19	78.1	21.9
600℃	3.5E20	8.7E18	97.5	2.5
800℃	3.1E20	3.1E19	90.0	10.0
1000℃	2.3E20	2.1E19	90.9	9.1

Table 5. Comparison of N values between the superparamagnetic and ferromagnetic-like components of the temperature annealed series.

Sample	Superparamagnetic M_S (emu/g)	Ferromagnetic-like M_S (emu/g)	% Superparamagnetic Contribution	% Ferromagnetic-like Contribution
400℃	0.06607	0.02381	63.96	36.04
600℃	0.08355	0.02571	69.23	30.77
800℃	0.06257	0.02336	62.67	37.33
1000℃	0.04503	0.01563	65.29	34.71

Table 6. Comparison of M_S values between the superparamagnetic and ferromagnetic-like components of the temperature annealed series.

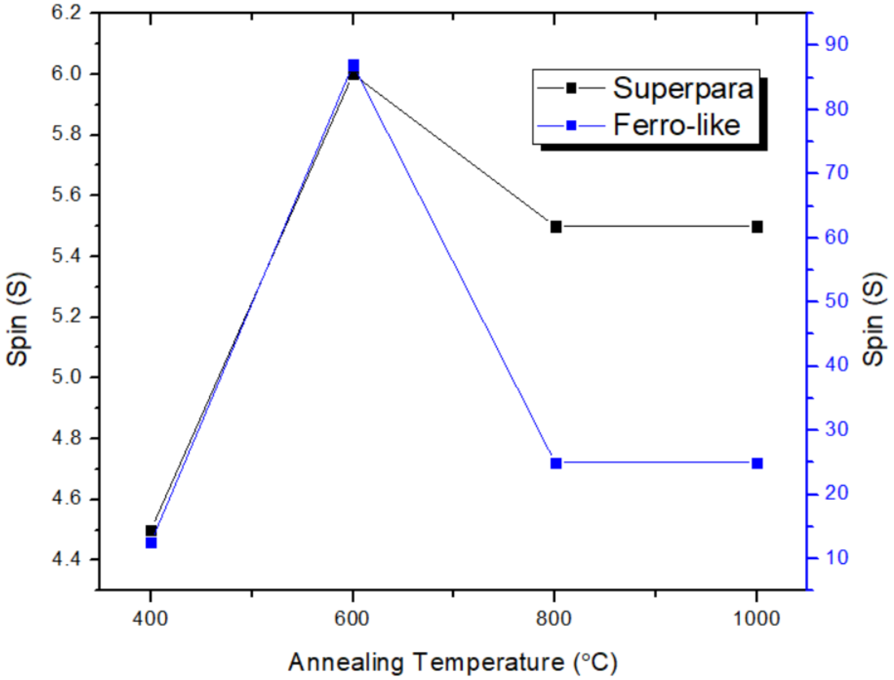

Figure 37. Spin values (S) of temperature annealing series.

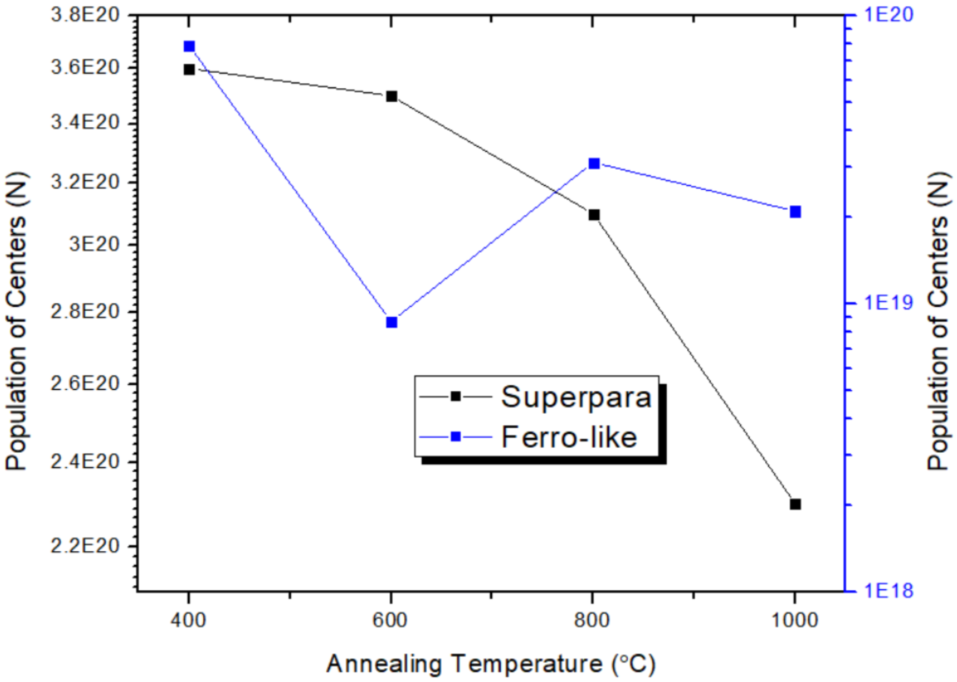

Figure 38. Population of centers (N) of temperature annealing series.

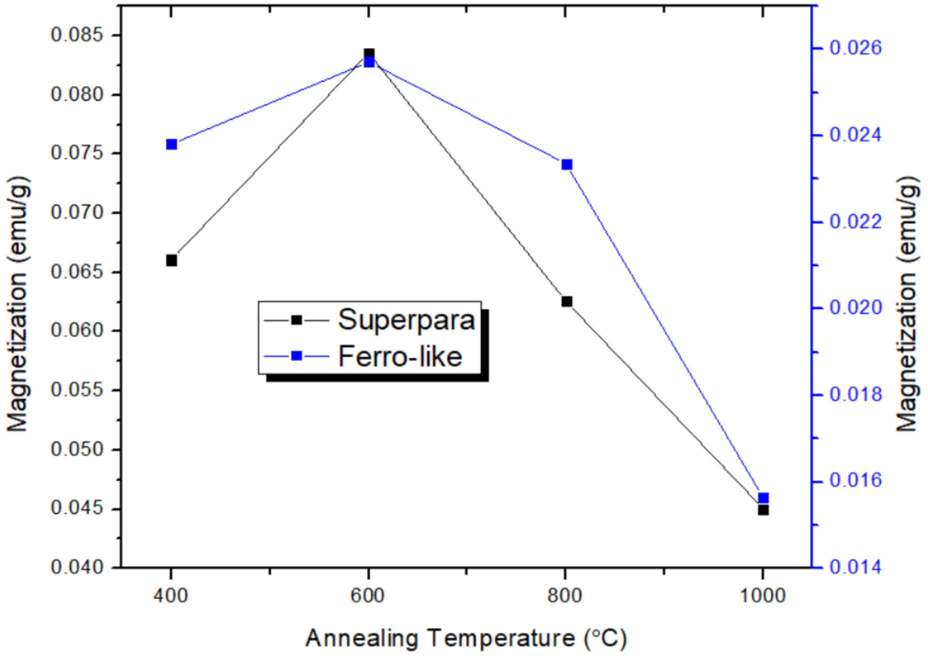

Figure 39. Magnetization (M_S) of temperature annealing series.

Looking at the above tables and graphs, the 600˚C sample had the highest spin for both its superparamagnetic and ferromagnetic-like components (S=6 and S=87, respectively). Initially the spin greatly increased from 400˚C to 600˚C, but then above 600˚C the spin fell to a plateau where it stabilized. This might have been caused by the clustering of migrating defects into clusters with low population (%N of ferromagnetic-like centers = 2.5%) but with very high spin and magnetization (0.02571 emu/g). Since from the XRD, 400˚C was unable to properly sinter the crystals together, but 600˚C provided enough energy to form Ce-O bonds and for defects to migrate through the lattice into clusters. This is also supported how the spin and magnetization decreased as the temperature increased above 600˚C, due to oxygen vacancies being filled in and lowering the concentration of contributing defects. However, it should also be considered that the ionic conductivity of CeO_2 will increase as the grain size increases, and the frequency of charge transfer from oxygen species to the Ce 4f mid-band gap states would also increase.[34,44,55]

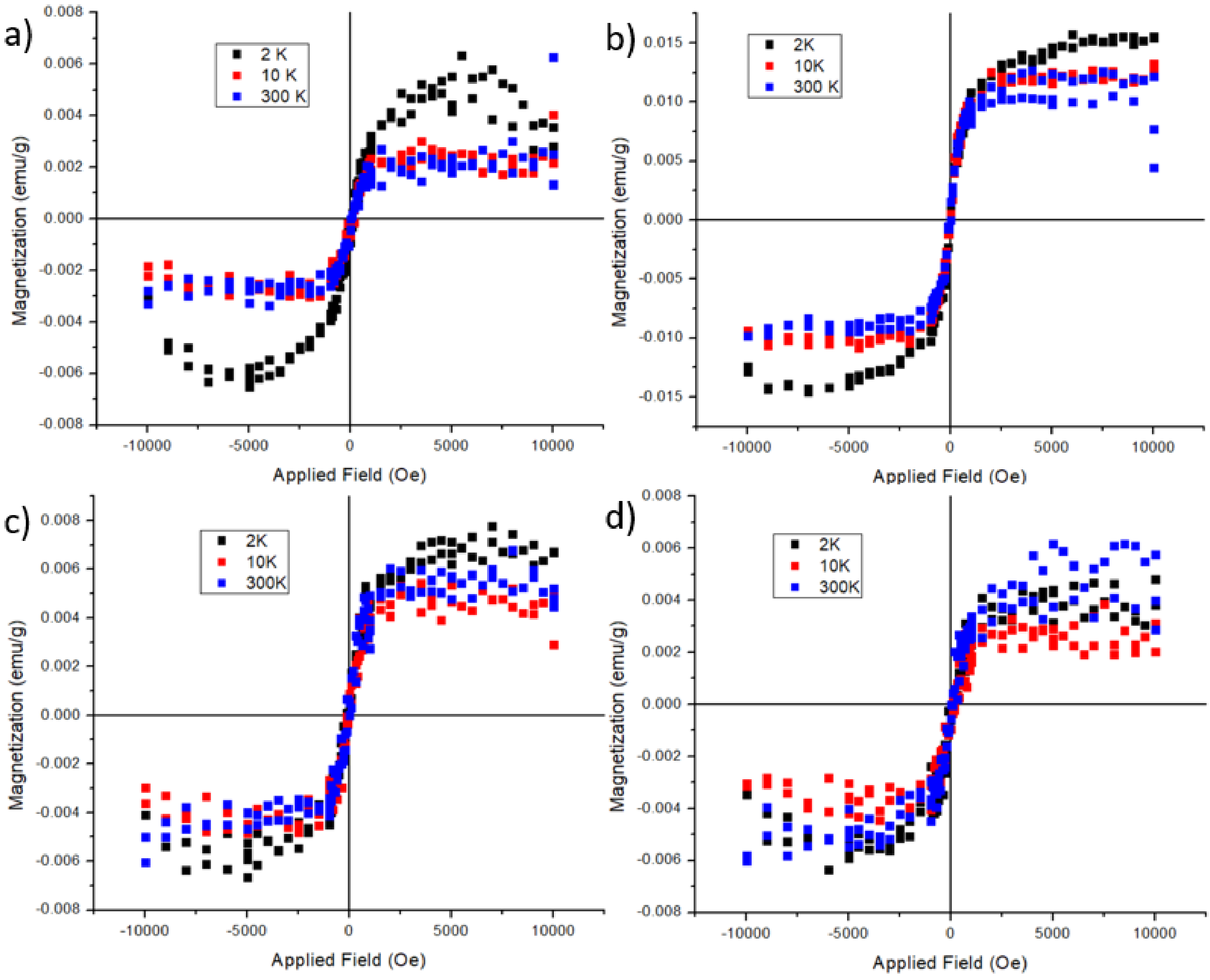

Figure 40. Magnetic sweep measurements between -1 to 1 T of CeO_{2-X} annealed for 24 hr at a) 400℃, b) 600℃, c) 800℃, and d) 1000℃.

After removing the paramagnetic and/or diamagnetic components, all samples showed a ferromagnetic-like response at 300 K. The magnetic signal barely changed as the temperature decreased from 300 K to 2 K for the 800°C and 1000°C samples, and between 300 K and 10 K for the 400°C and 600°C samples. It appears the crystal size is impacting the magnetic behaviour since the smaller sized 400°C and 600°C samples have increased signal from 10 K to 2 K but not for the larger samples. So the superparamagnetic component is stronger when the crystal size is smaller, while the ferromagnetic-like component generally increases when the crystal size is larger. Which means the ferromagnetic-like component is somehow related to the type of conductivity.

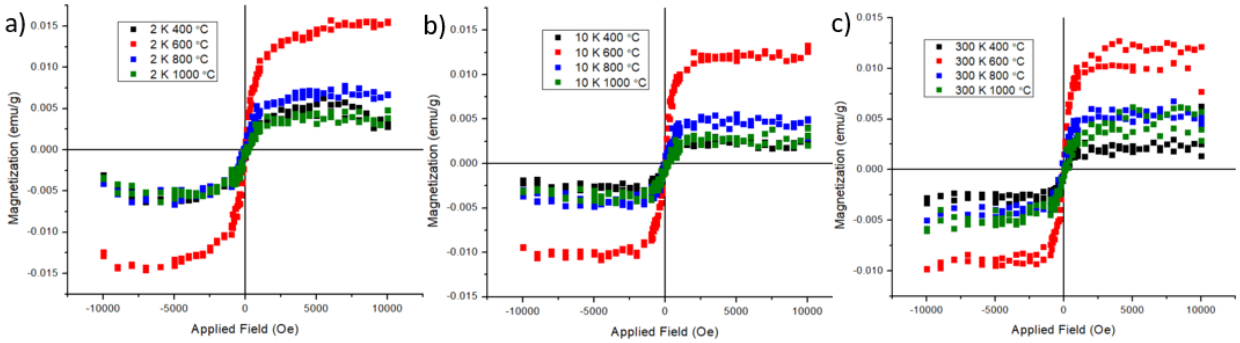

Figure 41. Comparison of magnetic sweep data of CeO_{2-X} temperature annealed series measured at a) 2 K and b) 10 K, and c) 300 K. Black is 400°C, red is 600°C, blue is 800°C, and green is 1000°C.

Overall, all temperatures had a ferromagnetic-like signal at 300 K, but the size of its contribution varied depending on the annealing temperature. 600°C annealing temperature showed the highest M_S and spin values and strongest ferromagnetic-like behaviour at 300 K as shown in Figure 41.c). Consistently, 600 C also showed the highest magnetic response at 2 K and 10 K. It was found there were two properties that controlled the total magnetic signal: clustering of Ce^{3+}/oxygen vacancy defects and grain size/type of conductivity. Hence, the mechanism of both the superparamagnetic and ferromagnetic-like components is a combination of the two properties. The degree of how impactful the clustering of defects or grain size is on the magnetic signal is undecided, but it can be confirmed using MCD spectroscopy to find which species is causing the ferromagnetic-like ordering. Thus, 600˚C annealing was used as the control parameter for conducting the atmosphere annealing series experiments due to having the highest magnetic signal. Additionally, CeO_{2-X} annealed for 24 hr at 600˚C in air was chosen as one of the samples for studying the magneto-optical properties of annealed CeO_{2-X}.

4.3 Annealing Atmosphere Series

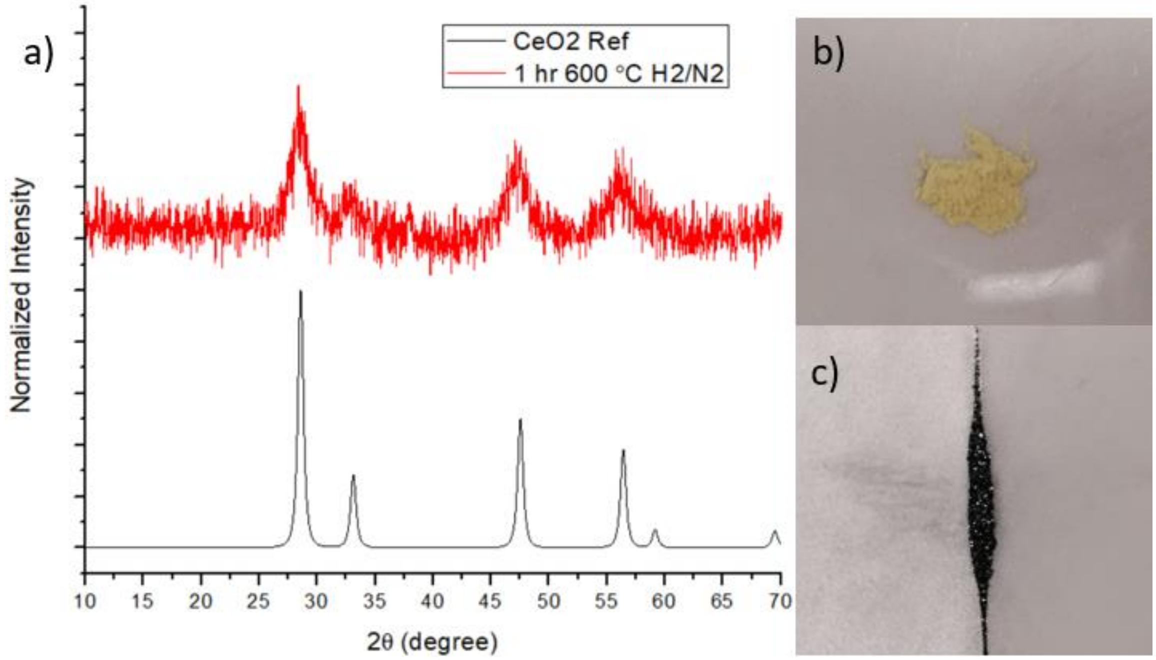

Figure 42. a) XRD of H_2/N_2 atmosphere annealed CeO_{2-X} at 600℃ for 1 hr. Physical appearance of CeO_{2-X} annealed at b) 600℃ 24 hr in air and c) 600℃ in H_2/N_2 for 1 hr.

The atmosphere annealing series was prepared by annealing CeO_{2-X} NCs made from the same batch as the temperature annealing series to control for the initial concentration of defects and to compare the two series. Initially, 24 hr annealing at 600°C under H_2/N_2 atmosphere was attempted to control for both the annealing time and temperature, but the sample reduced to Ce metal and became a black shiny crystalline powder. This was not unexpected, since most oxides will be reduced to metal under a reducing atmosphere at such a high temperature and long annealing time. A new sample was then prepared and annealed for 1 hr at 600°C under H_2/N_2. After annealing, the 1 hr sample also became a black shiny powder like the 24 hr annealed sample. So XRD was collected and showed that the 600°C 1 hr under H_2/N_2 sample did not reduce to Ce metal but retained the cubic fluorite CeO_2 structure, albeit with broader peaks due to the short annealing time as shown in Figure 42.a).

In literature, black CeO_{2-X} has been reported, and like black TiO_2, is known to turn blue/black in a very oxygen deficient environment where so much oxygen is missing that black CeO_{2-X} begins to have metallic-like properties despite having a metal oxide structure.[36,37] So, by reducing CeO_{2-X} with H_2/N_2, black CeO_{2-X} was likely synthesized.

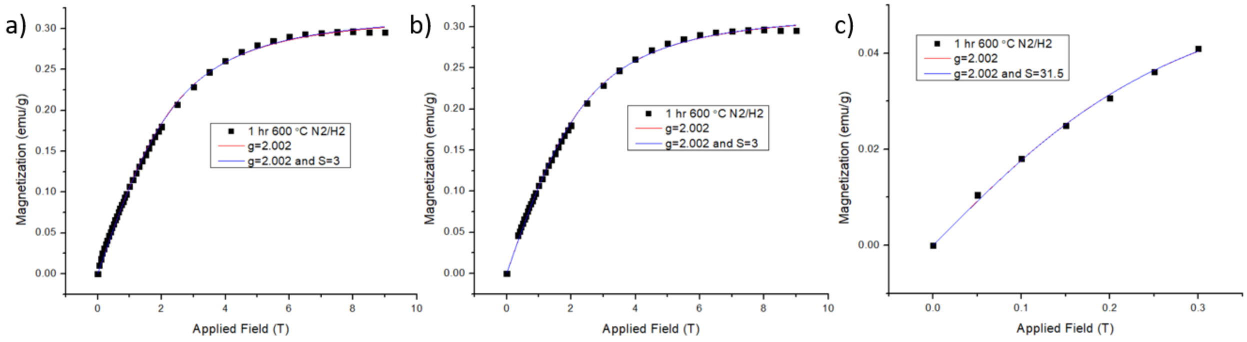

Figure 43. Magnetic saturation curves measured at 2 K between 0-9 T for a) combined data, b) isolated superparamagnetic component, and c) isolated ferromagnetic-like component of CeO_{2-X} annealed at 600℃ 1 hr under H_2/N_2.

Sample	Superparamagnetic S	Ferromagnetic-like S
1 hr 600˚C N2/H2	3	31.5
24 600˚C Air	6	87

Table 7. Comparison of spin values between the superparamagnetic and ferromagnetic-like components of the atmosphere annealed series.

Sample	Superparamagnetic N	Ferromagnetic-like N	% Superparamagnetic Contribution	% Ferromagnetic-like Contribution
1 hr 600˚C N2/H2	2.8E21	5.5E19	98.0	2.0
24 600˚C Air	3.5E20	8.7E18	97.5	2.5

Table 8. Comparison of N values between the superparamagnetic and ferromagnetic-like components of the atmosphere annealed series.

Sample	Superparamagnetic M_S (emu/g)	Ferromagnetic-like M_S (emu/g)	% Superparamagnetic Contribution	% Ferromagnetic-like Contribution
1 hr 600̊C N2/H2	0.29572	0.041023	86.13	13.87
24 600 ˚C Air	0.08355	0.02571	69.23	30.77

Table 9. Comparison of M_S values between the superparamagnetic and ferromagnetic-like components of the atmosphere annealed series.

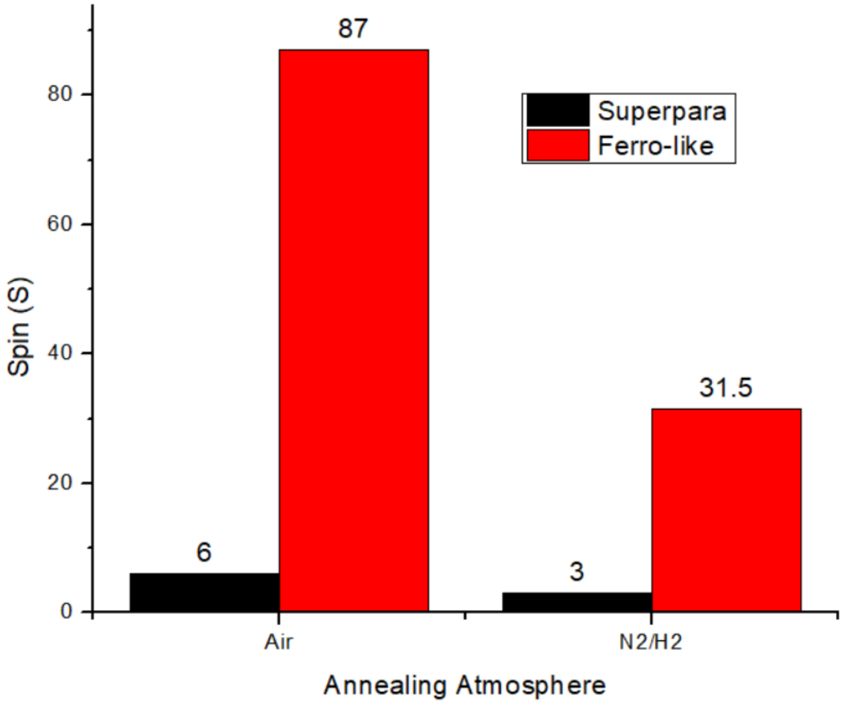

Figure 44. Comparison of spin values (S) between 1 hr H_2/N_2 annealed CeO_{2-X} and 24 hr 600̊C air annealed CeO_{2-X}.

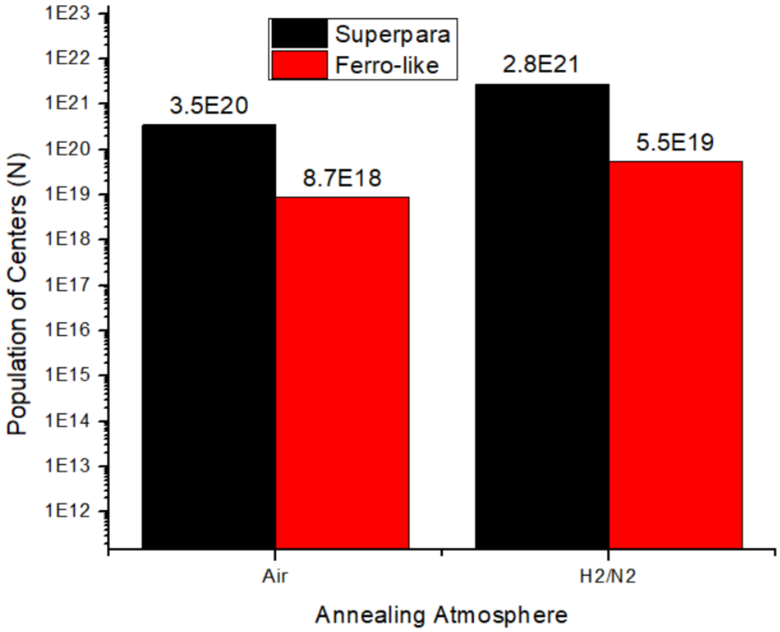

Figure 45. Comparison of population of centers (N) between 1 hr H_2/N_2 annealed CeO_{2-X} and 24 hr 600℃ air annealed CeO_{2-X}.

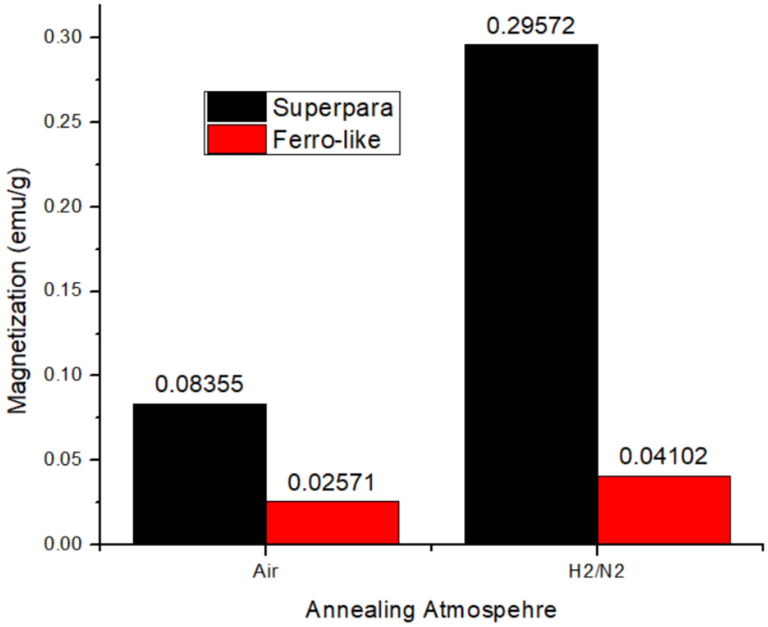

Figure 46. Comparison of magnetization (M_S) between 1 hr H_2/N_2 annealed CeO_{2-X} and 24 hr 600℃ air annealed CeO_{2-X}.

Comparing the above magnetic saturation data between H_2/N_2 and air annealed CeO_{2-X}, it was found that the air annealed sample had higher S for both components, but the H_2/N_2 annealed sample had higher N and M_S. Most of the magnetic saturation found in the H_2/N_2 sample was caused by a larger superparamagnetic component due to having a higher concentration of Ce^{3+} defects than the air annealed CeO_{2-X}. However, the air annealed sample had a higher ferromagnetic-like percentage contribution to its total magnetic response (air = 30.77% vs H_2/N_2 = 13.87%). If the room-temperature ferromagnetic-like ordering was caused more by the clustering of defects, then the H_2/N_2 annealed sample would have a larger ferromagnetic-like percentage contribution. Instead having more defects only increased the superparamagnetic component.

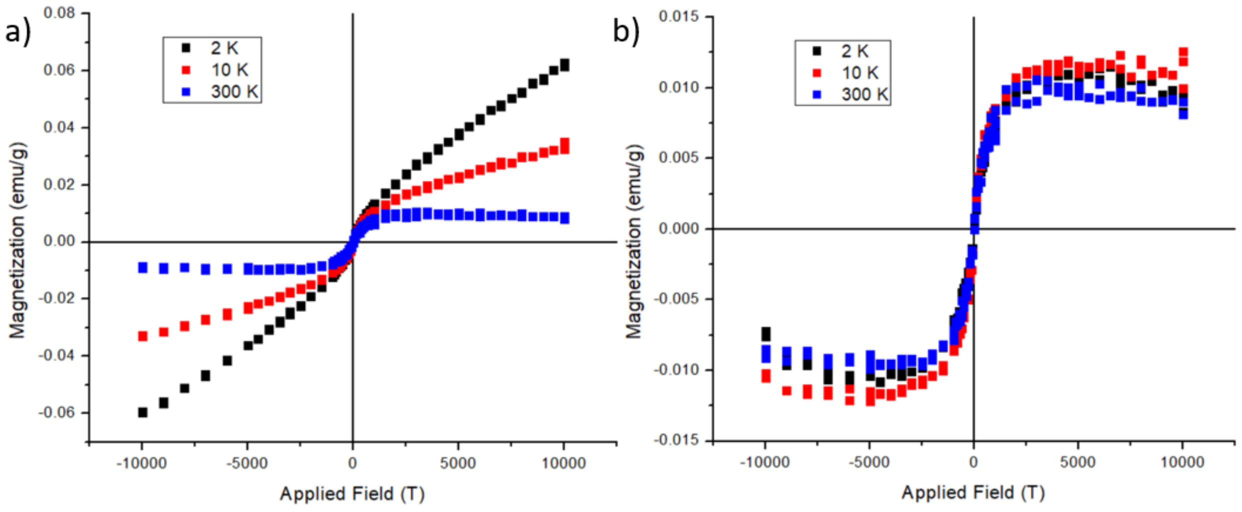

Figure 47. Magnetic sweep measurements between -1 to 1 T of a) raw data and b) corrected data for CeO_{2-X} annealed at 600℃ for 1 hr under H_2/N_2.

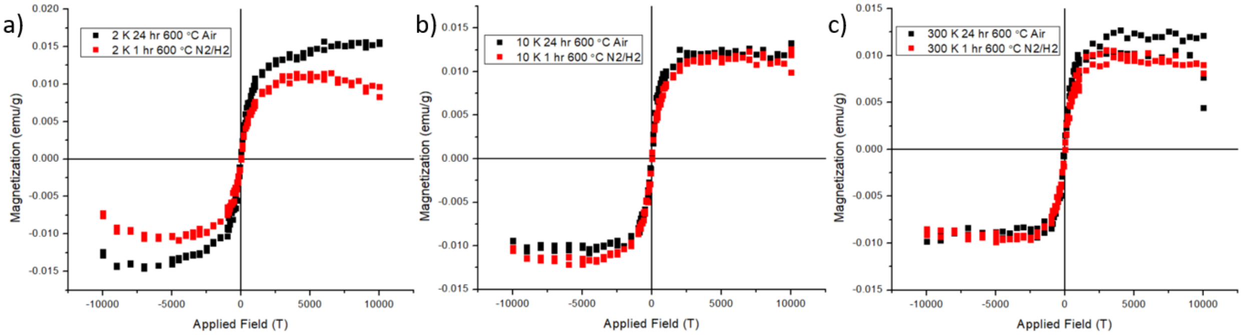

Figure 48. Magnetic sweep measurements between -1 to +1 T comparing CeO_{2-X} annealed in air (black) vs H_2/N_2 (red) at a) 2 K, b) 10 K, and c) 300 K.

Magnetic sweep measurements were collected for CeO_{2-X} annealed in H_2/N_2 for 1 hr at 600 ˚C and then compared with CeO_{2-X} annealed in air for 24 hr at 600˚C. It was found that at each temperature, both samples had very similar magnetic intensities and a ferromagnetic-like response that barely changed from 300 K to 2 K. To add, air annealed CeO_{2-X} had slightly higher magnetic response at 300 K and 2 K. Because the air and H_2/N_2 samples had similar intensities, it proved that having a higher concentration of defects does not enhance the ferromagnetic-like ordering. Thus, the concentration of defects only plays an indirect role in the mechanism behind the ferromagnetic-like ordering, while grain size and conductivity type play an important role. For the final section of this chapter, 1 hr annealed CeO_{2-X} at 600˚C in H_2/N_2 was selected to help determine the species causing the ferromagnetic-like ordering using MCD spectroscopy and contrasted with air annealed CeO_{2-X}.

4.4 Magneto-optical Properties of Annealed CeO_{2-X}

For the final experiments that will be covered, CeO_{2-X} annealed at 600˚C for 24 hr in air and 600 ˚C for 1 hr under H_2/N_2 samples were studied using MCD spectroscopy. The goal of these experiments was to further characterize the electronic structure of CeO_{2-X} and to find the optical transitions with the same field dependent magnetic saturation that was found in the PPMS data. By doing so, we can pinpoint the exact species and site that it occupies to find the mechanism causing the d^0 ferromagnetic-like behaviour in CeO_{2-X}.

In Figure 49., field dependent MCD data was collected for air annealed CeO_{2-X}. Instead having multiple peaks like from the colloidal CeO_{2-X} MCD data, a single large broad MCD peak with positive parity at 339 nm was present. It was interesting how the MCD peak was below the first absorption peak in UV-vis which suggests the peak is correlated to sub band gap states. However, the energy of the 339 nm MCD peak is 3.66 eV and this roughly matches the energy of the first band gap transition from O 2p to Ce 4f (unoccupied) which is about 3.5 eV. Then using the Brillouin function, the integrated MCD peak intensity deviated from a fitting of g=2.002 and S=0.5 and showed linear field dependence. To note, having linear field dependence means the transition is not associated with Curie-type paramagnetism/behaviour. In other systems, linear dependence can be produced by the cyclotron motion of free electrons.[50] Which implies the transition is somehow delocalized in nature and temperature dependent MCD is required to determine if the peak is A- or B-term. Considering this, the MCD peak at 339 nm is likely a delocalized transition involving either electrons trapped in oxygen vacancies below the band gap or O 2p valence electrons transferring to the Ce 4f mid gap states.

In Figure 50., magnetic sweep measurements were conducted between -1 to +1 T with 0.2 T intervals in the range of 220 to 400 nm to mimic the parameters used from the PPMS measurements. However, after plotting integrated MCD intensity with respect to applied field there was no magnetic saturation and the data showed linear dependence like the prior measurements from 1 to 7 T.

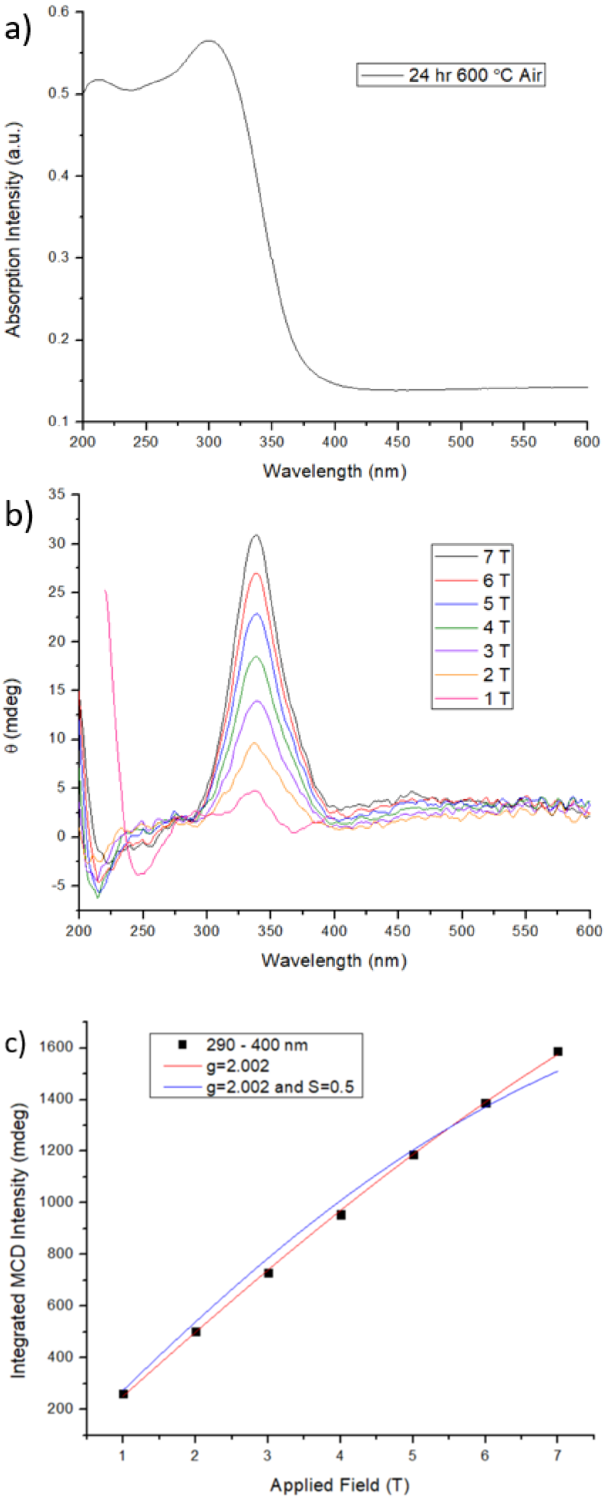

Figure 49. Field dependent MCD data of CeO_{2-X} annealed at 600˚C for 24 hr in air. a) UV-vis absorption data, b) MCD spectra collected at 5 K and c) field dependent plotted MCD intensity.

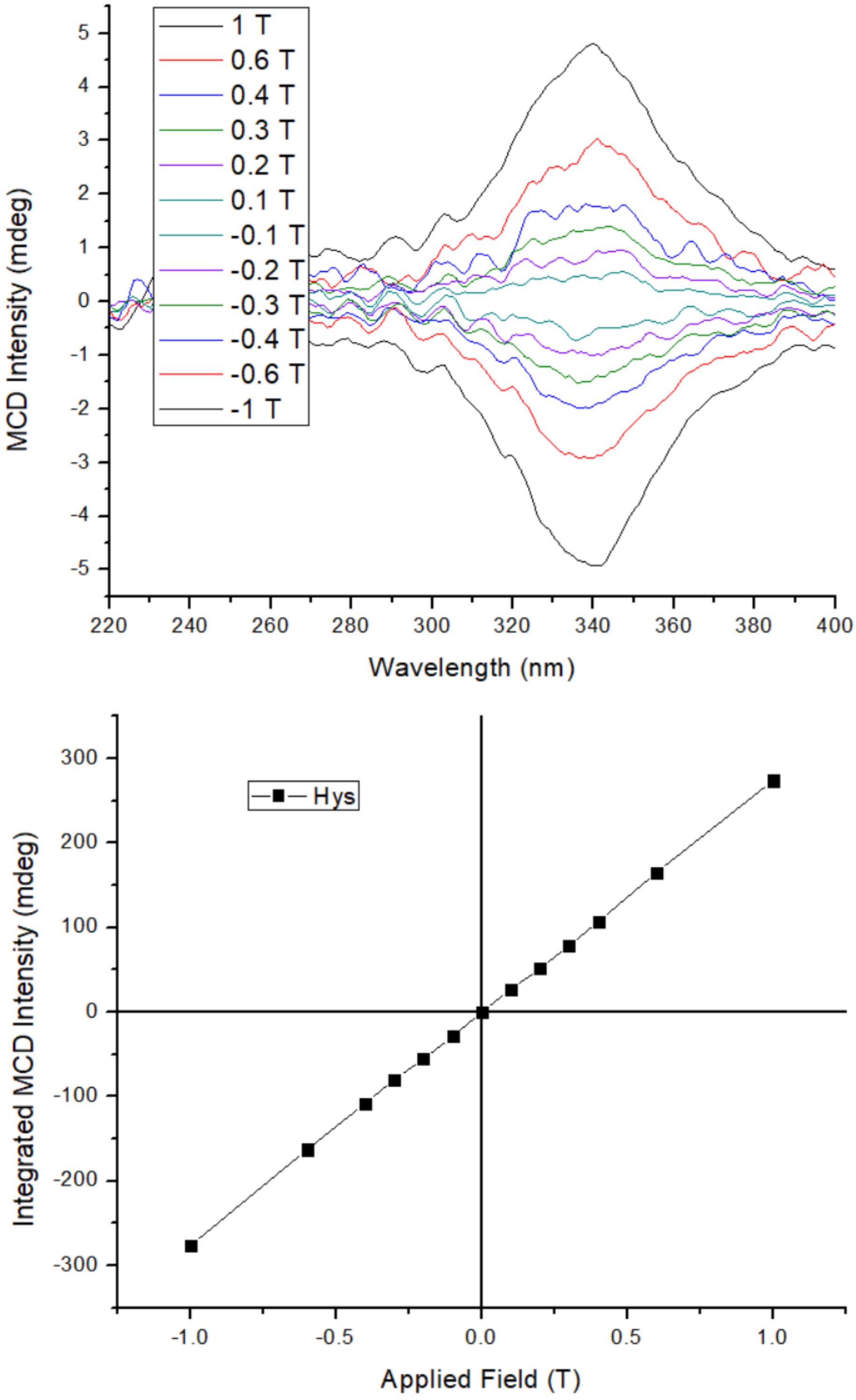

Figure 50. (above) Magnetic sweep measurements between -1 to +1 T using MCD for air annealed CeO_{2-X} collected at 5 K, (below) field dependent integrated MCD peak intensity from 290-400 nm.

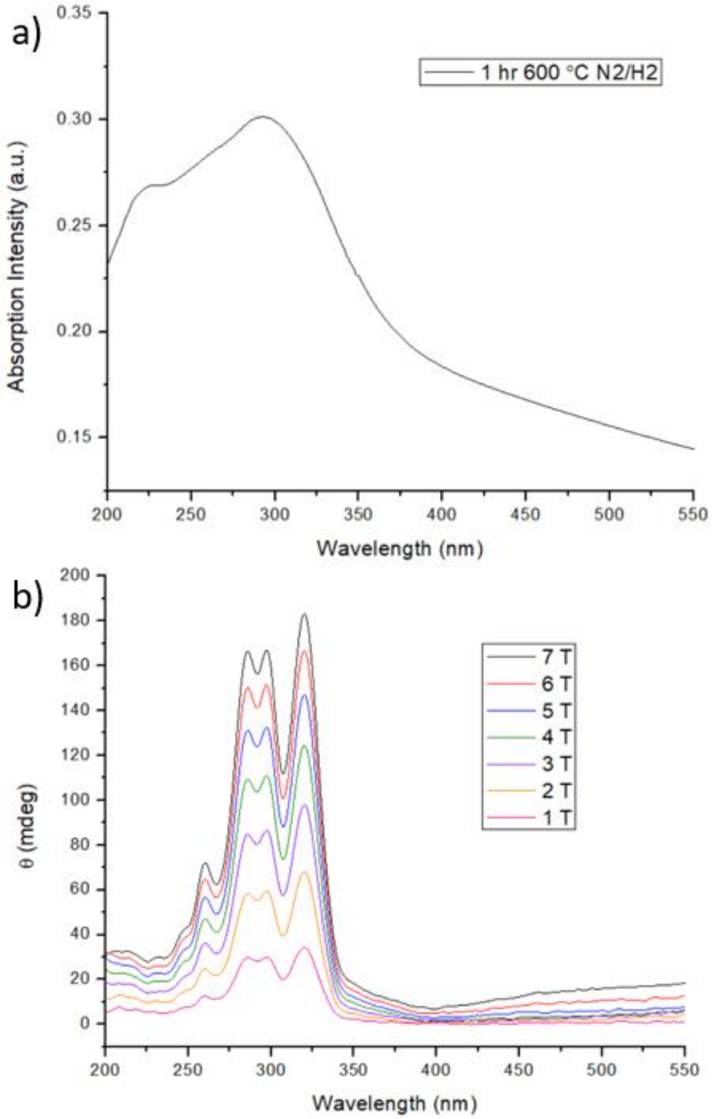

Figure 51. a) UV-vis absorption spectra of H_2/N_2 annealed CeO_{2-X}, and b) MCD field dependent spectra collected between 1 to 7 T at 5 K.

Next, field dependent MCD was conducted on the H_2/N_2 annealed sample from 1 to 7 T at 5 K. Shown in Figure 51, several defined peaks overlapped the same positions found in the colloidal CeO_{2-X} (282 nm peak, 215-260 nm and 315-400 nm broad regions) sample and the peaks were visibly saturating. The signal in the range between 400 to 550 nm was from the quartz substrate.

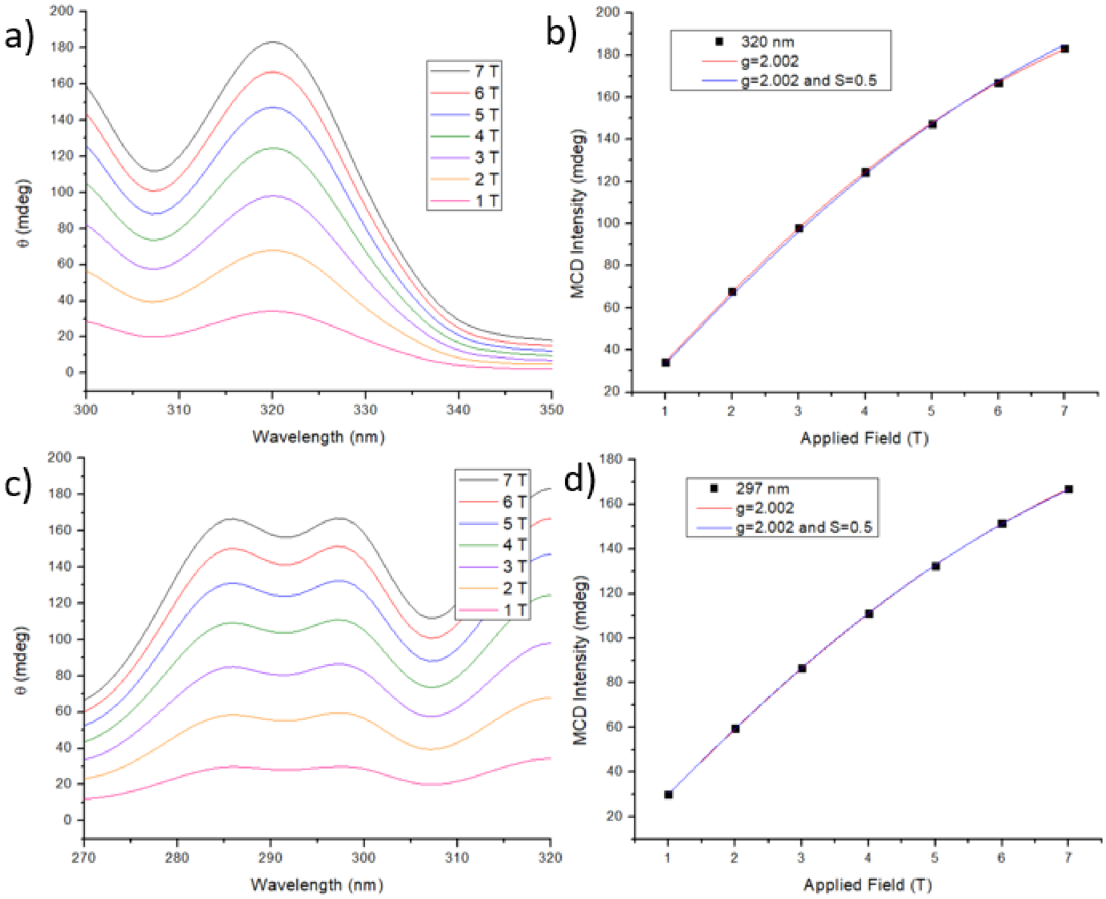

Figure 52. a) Field dependent MCD spectra of the 320 nm peak, b) plotted and fitted MCD intensity of the 320 nm peak, c) field dependent MCD spectra of the 297 nm peak, and d) plotted and fitted MCD intensity of the 297 nm peak.

In figure 52, the 320 nm and 297 nm MCD peaks and their field dependent MCD peak intensity plots are presented. For the 320 nm peak, the fitted values were g=2.002 and S=0.5, suggesting the transition is paramagnetic and likely a C-term. While for the 297 nm peak, again the fitted values were g=2.002 and S=0.5, showing this transition is also paramagnetic and likely a C-term.

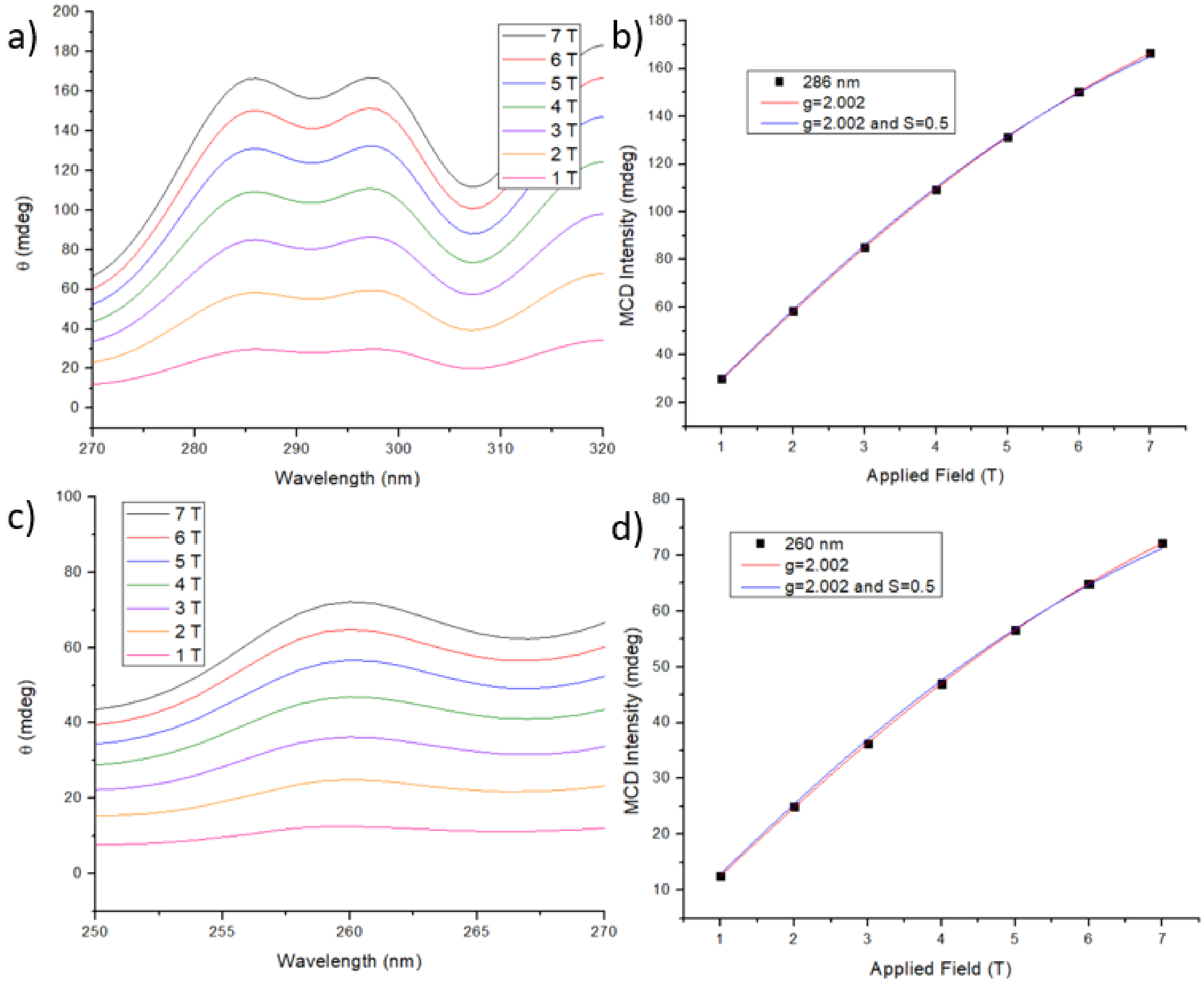

Figure 53. a) Field dependent MCD spectra of the 286 nm peak, b) fitted and plotted MCD peak intensity of the 286 nm peak, c) field dependent MCD spectra of the 260 nm peak, and d) fitted and plotted MCD peak intensity of the 260 nm peak.

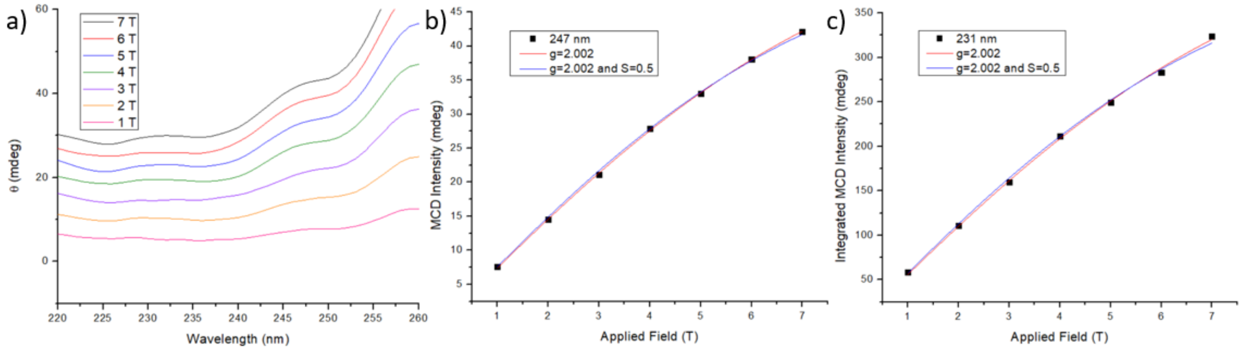

Figure 54. a) Field dependent MCD spectra of the 247 and 231 nm peaks, b) fitted and plotted MCD peak intensity of the 247 nm peak, and c) fitted and plotted integrated MCD peak intensity of the 231 nm peak.

Just like for the previous two peaks, the 286 nm, 260 nm, and 247, and 231 nm peaks each had values of g=2.002 and S=0.5, making them all paramagnetic and possibly C-terms. It should be noted that all the peak positions were nearly the same as the colloidal CeO_{2-X} peaks and only shifted by a few nm. The 320 nm peak is mostly likely the same transition found at 339 nm in air annealed CeO_{2-X} but is blueshifted and does not have linear dependence. The redshifted 339 nm peak might be due to the air annealed CeO_{2-X} sample having bulk crystals, while the H_2/N_2 annealed CeO_{2-X} sample is nanocrystalline and under the quantum confinement effect. Meanwhile, the rest of the peaks in H_2/N_2 annealed CeO_{2-X} can be used to deconvolute the broad shoulder regions in the colloidal CeO_{2-X} sample. The stronger signals found in the H_2/N_2 annealed sample are probably caused by having a large concentration of Ce^{3+} defects that have molecular electronic structure. Finally, just like the air annealed sample, the magnetic saturation found in the PPMS data was not observed in the MCD spectra.

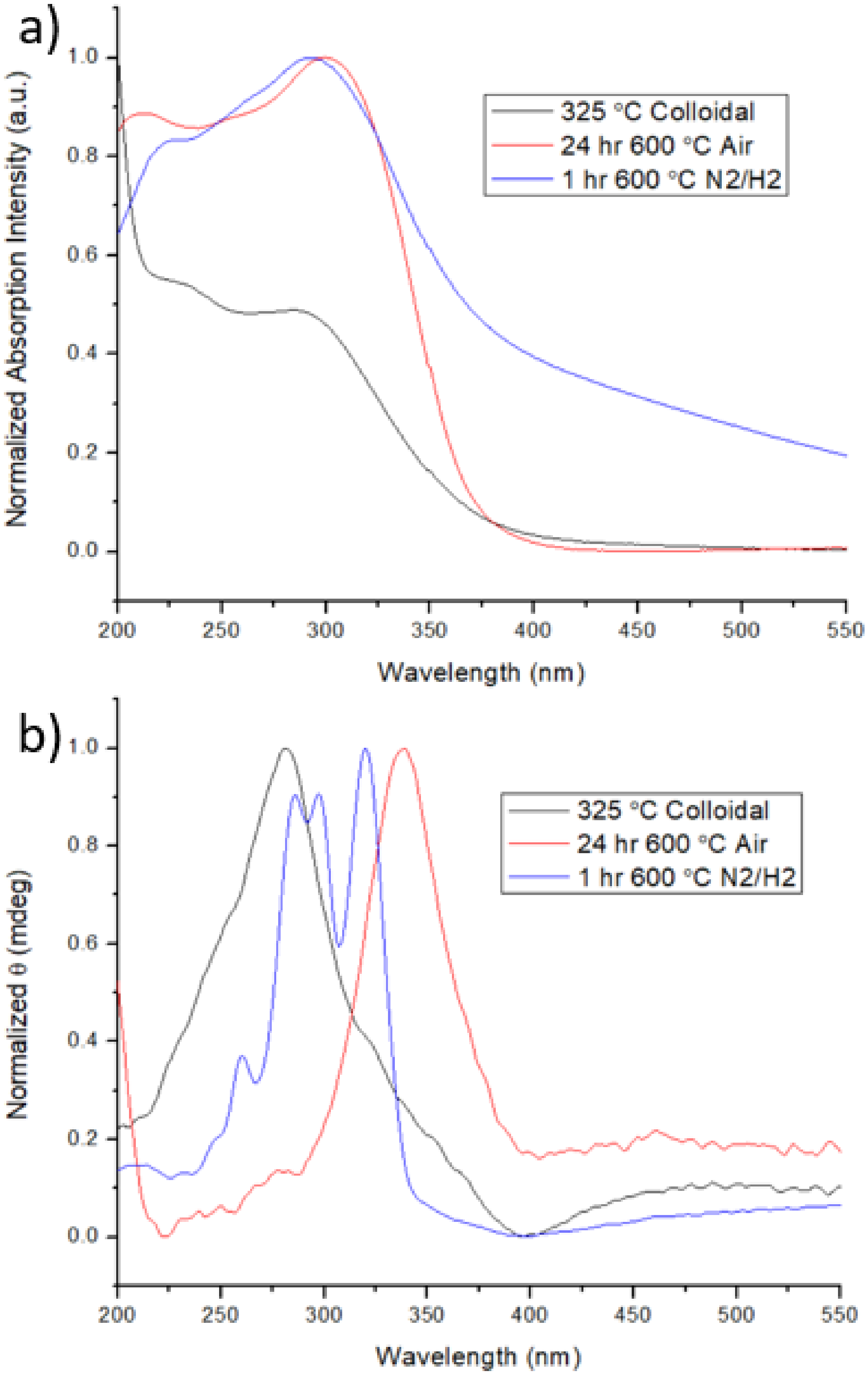

Figure 55. a) Normalized UV-vis absorption data of for all samples and b) field dependent MCD spectra of all samples at 5 K 7 T.

The field dependent MCD spectra measured at 5 K 7 T and UV-vis absorption spectra of all samples were normalized to compare the peak positions. The MCD peaks of the H_2/N_2 annealed CeO_{2-X} and colloidal CeO_{2-X} samples overlapped, where the H_2/N_2 annealed sample could be used to deconvolute the broad regions of the colloidal sample from 215-260 nm and 315-400 nm. It was found that both samples had multiple transitions that fitted for g=2.002 and S=0.5 and are likely C-terms due to being paramagnetic. Except, the 315-400 nm region of the colloidal sample and the 339 nm peak of the air annealed CeO_{2-X} both deviated from a Brillouin fit of g=2.002 and S=0.5 and showed linear dependence. This implied that the 315-400 nm region and 339 nm peak are delocalized in nature since in other systems the cyclotron motion of free electrons also show linear dependence. On top of this, the 320 nm peak of the H_2/N_2 annealed sample did not show linear dependence. Now connecting to the PPMS data, the ferromagnetic-like component was more impacted by the grain size/conductivity type of the sample, while having a higher concentration of Ce^{3+}/oxygen vacancy defects only increased the superparamagnetic component. Which suggests that the origin of the d^0 ferromagnetic-like ordering in CeO_2 is caused by the delocalized transition at 339 nm and annealing CeO_2 at 600˚C in air for 24 hr enhances this transition.

In summary, the mechanism causing the d^0 ferromagnetic-like ordering in CeO_2 is likely from a delocalized charge transfer occurs from either trapped electrons in oxygen vacancies or O 2p valence electrons to the Ce 4f (unoccupied) mid-band gap states. The magnetic ordering occurs when the electron transfer can increase the Fermi level to a peak in the local density of states causing Stoner splitting of the total density of states. Finally, Stoner splitting then causes spin polarization of the density of states into an uneven number of up or down spins, creating an overall net magnetic moment. Another evidence that supports the proposed mechanism is the temperature independent ferromagnetic-like component observed in the PPMS data, and charge transfer-mediated magnetism is known not to follow Curie-type behaviour. Therefore, the d^0 ferromagnetic-like ordering in CeO_2 is likely caused by charge transfer-mediated magnetism.

Chapter 5

Concluding Statements and Future Work

5.1 Conclusions

In conclusion, the structural, electronic, magnetic, and magneto-optical properties of CeO_{2-X} NCs and bulk powders were investigated to determine the mechanism causing the room temperature ferromagnetic-like behaviour reported in literature, and to provide further insight to the current debate. It was found that the origin of the d^0 ferromagnetic-like ordering in undoped CeO_2 is likely caused by charge transfer-mediated magnetism. Where a delocalized charge transfer occurs from either electrons trapped in oxygen vacancies or O 2p valence electrons to Ce 4f mid-band gaps states causes Stoner splitting to polarize the spins at the Fermi level, creating an uneven number of unpaired spins, and an overall net magnetic moment. The magnetic ordering can be enhanced by annealing CeO_2 into bulk powders, where the magnetic signal is controlled directly by the grain size of the crystals and indirectly supported by the concentration of Ce^{3+}/oxygen vacancy defects.

5.2 Future Work

To confirm this theory, further characterization using temperature dependent XRD, SEM analysis of different grain sizes, additional PPMS data to extrapolate the Curie temperature of the superparamagnetic component, and temperature dependent MCD is necessary. If more analysis is collected the proposed mechanism behind the d^0 room-temperature ferromagnetic-like behaviour can ultimately be confirmed and CeO_{2-X} could become an excellent candidate material for spintronic applications.

References

1. Cheng, S. J. Theory of magnetism in diluted magnetic semiconductor nanocrystals. *Phys. Rev. B - Condens. Matter Mater. Phys.* **77**, 1–8 (2008).
2. Dietl, T. A ten-year perspective on dilute magnetic semiconductors and oxides. *Nat. Mater.* **9**, 965–974 (2010).
3. Shi, H., Hussain, T., Ahuja, R., Kang, T. W. & Luo, W. Role of vacancies, light elements and rare-earth metals doping in CeO 2. *Sci. Rep.* **6**, 1–8 (2016).
4. Garnet, N. S. *et al.* Probing the role of dopant oxidation state in the magnetism of diluted magnetic oxides using Fe-doped In2O3 and SnO2 nanocrystals. *J. Phys. Chem. C* **121**, 1918–1927 (2017).
5. Prellier, W., Fouchet, A. & Mercey, B. Oxide-diluted magnetic semiconductors: A review of the experimental status. *J. Phys. Condens. Matter* **15**, (2003).
6. Spaldin, N. A. *MAGNETIC MATERIALS Fundamentals and Applications*. (Cambridge University Press, 2012).
7. Wolf, S. A. *et al.* Spintronics: A spin-based electronics vision for the future. *Science (80-.).* **294**, 1488–1495 (2001).
8. Ju, L. *et al.* Interplay between size, composition, and phase transition of nanocrystalline Cr 3+-doped BaTiO 3 as a path to multiferroism in perovskite-type oxides. *J. Am. Chem. Soc.* **134**, 1136–1146 (2012).
9. Ning, S., Zhan, P., Xie, Q., Wang, W. & Zhang, Z. Defects-driven ferromagnetism in undoped dilute magnetic oxides: A Review. *J. Mater. Sci. Technol.* **31**, 969–978 (2015).
10. Rashad, M. Tuning optical properties of polyvinyl alcohol doped with different metal oxide nanoparticles. *Opt. Mater. (Amst).* **105**, 109857 (2020).
11. Islam, M. A. *et al.* Alkaline and rare-earth metals doped transparent conductive tin oxide thin films. *J. Sol-Gel Sci. Technol.* **96**, 304–313 (2020).

12. Hummel, R. E. *Electronic Properties of Materials*. (Springer Science: Business Media, LLC, 2011). doi:0.1007/978-1-4419-8164-6

13. Ma, Z., Mohapatra, J., Wei, K., Liu, J. P. & Sun, S. Magnetic Nanoparticles: Synthesis, Anisotropy, and Applications. *Chem. Rev.* **123**, 3904–3943 (2023).

14. Sytnyk, M. *et al.* Tuning the magnetic properties of metal oxide nanocrystal heterostructures by cation exchange. *Nano Lett.* **13**, 586–593 (2013).

15. Li, X. *et al.* Spin hamiltonians in magnets: Theories and computations. *Molecules* **26**, 1–26 (2021).

16. Bhattacharjee, C. R., Purkayastha, D. D. & Chetia, J. R. Surfactant-assisted low-temperature thermal decomposition route to spherical NiO nanoparticles. *J. Coord. Chem.* **64**, 4434–4442 (2011).

17. Wang, T. & Radovanovic, P. V. Free electron concentration in colloidal indium tin oxide nanocrystals determined by their size and structure. *J. Phys. Chem. C* **115**, 406–413 (2011).

18. Manthiram, K. & Alivisatos, A. P. Tunable localized surface plasmon resonances in tungsten oxide nanocrystals. *J. Am. Chem. Soc.* **134**, 3995–3998 (2012).

19. Lawrence, N. J. *et al.* Defect engineering in cubic cerium oxide nanostructures for catalytic oxidation. *Nano Lett.* **11**, 2666–2671 (2011).

20. López-Ortega, A., Lottini, E., Fernández, C. D. J. & Sangregorio, C. Exploring the Magnetic Properties of Cobalt-Ferrite Nanoparticles for the Development of a Rare-Earth-Free Permanent Magnet. *Chem. Mater.* **27**, 4048–4056 (2015).

21. Kim, K. *et al.* Synthetic Control of Intrinsic Defect Formation in Metal Oxide Nanocrystals Using Dissociated Spectator Metal Salts. *J. Am. Chem. Soc.* **144**, 22941–22949 (2022).

22. Wang, Z. *et al.* Dependence of the Ferromagnetism on Vacancy Defect in Annealed In2O3 Nanocrystals: A Positron Annihilation Study. *Phys. Status Solidi Appl. Mater. Sci.* **218**, 1–9 (2021).

23. Biadala, L. *et al.* Magnetic polaron on dangling-bond spins in CdSe colloidal nanocrystals. *Nat. Nanotechnol.* **12**, 569–574 (2017).

24. Agrawal, A. *et al.* Localized Surface Plasmon Resonance in Semiconductor Nanocrystals. *Chem. Rev.* **118**, 3121–3207 (2018).

25. Tang, F. L. *et al.* Dependence of magnetism on the doping level of Zn1-xMnxTe nanoparticles synthesized by a hydrothermal method. *RSC Adv.* **4**, 49308–49314 (2014).

26. Bandyopadhyay, A., Sarkar, B. J., Sutradhar, S., Mandal, J. & Chakrabarti, P. K. Synthesis, structural characterization, and studies of magnetic and dielectric properties of Gd3+ doped cerium oxide (Ce0.90Gd0.10O2−δ). *J. Alloys Compd.* **865**, 158838 (2021).

27. Coey, J. M. D., Wongsaprom, K., Alaria, J. & Venkatesan, M. Charge-transfer ferromagnetism in oxide nanoparticles. *J. Phys. D. Appl. Phys.* **41**, (2008).

28. Ying, M. *et al.* ZnO gap states investigated using magnetic circular dichroism. *J. Phys. D. Appl. Phys.* **48**, (2015).

29. Shyichuk, A. & Zych, E. Oxygen Vacancy, Oxygen Vacancy-Vacancy Pairs, and Frenkel Defects in Cubic Lutetium Oxide. *J. Phys. Chem. C* **124**, 14945–14962 (2020).

30. Farvid, S. S. *et al.* Evidence of charge-transfer ferromagnetism in transparent diluted magnetic oxide nanocrystals: Switching the mechanism of magnetic interactions. *J. Am. Chem. Soc.* **136**, 7669–7679 (2014).

31. Zhang, C., Yin, P., Lu, W., Galievsky, V. & Radovanovic, P. V. On the Origin of d0 Magnetism in Transparent Metal Oxide Nanocrystals. *J. Phys. Chem. C* **125**, 27714–27722 (2021).

32. Coey, J. M. D. Magnetism in d 0 oxides. *Nat. Mater.* **18**, 652–656 (2019).

33. Coey, M., Ackland, K., Venkatesan, M. & Sen, S. Collective magnetic response of CeO 2 nanoparticles. *Nat. Phys.* **12**, 694–699 (2016).

34. Paidi, V. K., Brewe, D. L., Freeland, J. W., Roberts, C. A. & Van Lierop, J. Role of Ce 4f hybridization in the origin of magnetism in nanoceria. *Phys. Rev. B* **99**, 4–8 (2019).

35. Kullgren, J., Castleton, C. W. M., Müller, C., Ramo, D. M. & Hermansson, K. B3LYP

calculations of cerium oxides. *J. Chem. Phys.* **132**, (2010).

36. Mogensen, M., Sammes, N. M. & Tompsett, G. A. Physical, chemical and electrochemical properties of pure and doped ceria. *Solid State Ionics* **129**, 63–94 (2000).

37. Sahoo, S. S., Mansingh, S., Babu, P. & Parida, K. Black titania an emerging photocatalyst: Review highlighting the synthesis techniques and photocatalytic activity for hydrogen generation. *Nanoscale Adv.* **3**, 5487–5524 (2021).

38. Buchanan, C. A., Herrera, D., Balasubramanian, M., Goldsmith, B. R. & Singh, N. Unveiling the Cerium(III)/(IV) Structures and Charge-Transfer Mechanism in Sulfuric Acid. *JACS Au* **2**, 2742–2757 (2022).

39. Parker, D., Suturina, E. A., Kuprov, I. & Chilton, N. F. How the Ligand Field in Lanthanide Coordination Complexes Determines Magnetic Susceptibility Anisotropy, Paramagnetic NMR Shift, and Relaxation Behavior. *Acc. Chem. Res.* **53**, 1520–1534 (2020).

40. Maslakov, K. I. *et al.* The electronic structure and the nature of the chemical bond in CeO2. *Phys. Chem. Chem. Phys.* **20**, 16167–16175 (2018).

41. Montini, T., Melchionna, M., Monai, M. & Fornasiero, P. Fundamentals and Catalytic Applications of CeO2-Based Materials. *Chem. Rev.* **116**, 5987–6041 (2016).

42. Lu, Y., Thompson, C., Kunwar, D., Datye, A. K. & Karim, A. M. Origin of the High CO Oxidation Activity on CeO2 Supported Pt Nanoparticles: Weaker Binding of CO or Facile Oxygen Transfer from the Support? *ChemCatChem* **12**, 1726–1733 (2020).

43. Wang, B. *et al.* Fast ionic conduction in semiconductor CeO2-δ electrolyte fuel cells. *NPG Asia Mater.* **11**, (2019).

44. Tschöpe, A. & Birringer, R. Grain size dependence of electrical conductivity in polycrystalline cerium oxide. *J. Electroceramics* **7**, 169–177 (2001).

45. Ansari, S. A. *et al.* Band gap engineering of CeO2 nanostructure using an electrochemically active biofilm for visible light applications. *RSC Adv.* **4**, 16782–16791 (2014).

46. Chang, J. & Waclawik, E. R. Colloidal semiconductor nanocrystals: Controlled synthesis and surface chemistry in organic media. *RSC Adv.* **4**, 23505–23527 (2014).

47. Nguyen, M. T. *et al.* Synergistic Effect of the Oleic Acid and Oleylamine Mixed-Liquid Matrix on Particle Size and Stability of Sputtered Metal Nanoparticles. *ACS Sustain. Chem. Eng.* **8**, 18167–18176 (2020).

48. Mourdikoudis, S. & Liz-Marzán, L. M. Oleylamine in nanoparticle synthesis. *Chem. Mater.* **25**, 1465–1476 (2013).

49. Mason, W. R. *A Practical Guide to Magnetic Circular Dichroism Spectroscopy*. *A Practical Guide to Magnetic Circular Dichroism Spectroscopy* (2006). doi:10.1002/9780470139233

50. Yin, P., Tan, Y., Fang, H., Hegde, M. & Radovanovic, P. V. Plasmon-induced carrier polarization in semiconductor nanocrystals. *Nat. Nanotechnol.* **13**, 463–467 (2018).

51. Zhang, J. *et al.* Structural characteristics of cerium oxide nanocrystals prepared by the microemulsion method. *Chem. Mater.* **13**, 4192–4197 (2001).

52. Prieur, D. *et al.* Size Dependence of Lattice Parameter and Electronic Structure in CeO2 Nanoparticles. *Inorg. Chem.* **59**, 5760–5767 (2020).

53. Graciani, J. *et al.* Comparative study on the performance of hybrid DFT functionals in highly correlated oxides: The case of CeO2 and Ce2O3. *J. Chem. Theory Comput.* **7**, 56–65 (2011).

54. Develos-Bagarinao, K. *et al.* Comparative studies of nanostructural and morphological evolution of CeO2 thin films induced by high-temperature annealing. *Nanotechnology* **18**, 1–9 (2007).

55. Zhu, H. *et al.* Charge transfer drives anomalous phase transition in ceria. *Nat. Commun.* **9**, 1–8 (2018).